

Towards an improved geological interpretation of airborne electromagnetic data: a case study from the Cuxhaven tunnel valley and its Neogene host sediments (northwest Germany)

D. Steinmetz¹, J. Winsemann^{1,*}, C. Brandes¹, B. Siemon², A. Ullmann^{2,3}, H. Wiederhold³ & U. Meyer²

¹ Institut für Geologie, Leibniz Universität Hannover, Callinstr. 30, 30167 Hannover, Germany

² Bundesanstalt für Geowissenschaften und Rohstoffe, Stilleweg 2, 30655 Hannover, Germany

³ Leibniz-Institut für Angewandte Geophysik, Stilleweg 2, 30655 Hannover, Germany

* Corresponding author. Email: winsemann@geowi.uni-hannover.de

Abstract

Airborne electromagnetics (AEM) is an effective technique for geophysical investigations of the shallow subsurface and has successfully been applied in various geological settings to analyse the depositional architecture of sedimentary systems for groundwater and environmental purposes. However, interpretation of AEM data is often restricted to 1D inversion results imaged on resistivity maps and vertical resistivity sections. The integration of geophysical data based on AEM surveys with geological data is often missing and this deficiency can lead to uncertainties in the interpretation process. The aim of this study is to provide an improved methodology for the interpretation of AEM data and the construction of more realistic 3D geological subsurface models. This is achieved by the development of an integrated workflow and 3D modelling approaches based on combining different geophysical and geological data sets (frequency-domain helicopter-borne electromagnetic data (HFEM), time-domain helicopter-borne electromagnetic data (HTEM), three 2D reflection seismic sections and 488 borehole logs). We used 1D inversion results gained from both HFEM and HTEM surveys and applied a 3D resistivity gridding procedure based on geostatistical analyses and interpolation techniques to create continuous 3D resistivity grids. Subsequently, geological interpretations have been performed by combining with, and validation against, borehole and reflection seismic data. To verify the modelling results and to identify uncertainties of AEM inversions and interpretation, we compared the apparent resistivity values of the constructed 3D geological subsurface models with those of AEM field measurements. Our methodology is applied to a test site near Cuxhaven, northwest Germany, where Neogene sediments are incised by a Pleistocene tunnel valley. The Neogene succession is subdivided by four unconformities and consists of fine-grained shelf to marginal marine deposits. At the end of the Miocene an incised valley was formed and filled with Pliocene delta deposits, probably indicating a palaeo-course of the River Weser or Elbe. The Middle Pleistocene (Elsterian) tunnel valley is up to 350 m deep, 0.8–2 km wide, and incised into the Neogene succession. The unconsolidated fill of the Late Miocene to Pliocene incised valley probably formed a preferred pathway for the Pleistocene meltwater flows, favouring the incision. Based on the 3D AEM resistivity model the tunnel-valley fills could be imaged in high detail. They consist of a complex sedimentary succession with alternating fine- and coarse-grained Elsterian meltwater deposits, overlain by glaciolacustrine (Lauenburg Clay Complex) and marine Holsteinian interglacial deposits. The applied approaches and results show a reliable methodology, especially for future investigations of similar geological settings. The 3D resistivity models clearly allow a distinction to be made between different lithologies and enables the detection of major bounding surfaces and architectural elements.

Keywords: 3D subsurface model, airborne electromagnetics, Cuxhaven, Neogene incised valley, Pleistocene tunnel valley, uncertainties, workflow

Introduction

Airborne electromagnetics (AEM) is an effective technique to investigate the shallow subsurface. It has successfully been applied in various geological settings to analyse the

depositional architecture (e.g. Jordan & Siemon, 2002; Huuse et al., 2003; Sandersen & Jørgensen, 2003; Paine & Minty, 2005; Jørgensen & Sandersen, 2006, 2009; Bosch et al., 2009; Steuer et al., 2009; Pryet et al., 2011; Burschil et al., 2012a,b; Klimke et al., 2013). AEM enables a fast geological overview mapping

of subsurface structures and allows different lithologies and pore water conditions to be distinguished (Siemon, 2005; de Louw et al., 2011; Burschil et al., 2012a). Inversion procedures are carried out to create resistivity-depth models (e.g. Siemon et al., 2009a,b), which are the basis for resistivity-depth sections and maps. Although this technique is a well-established method to improve geological interpretations of the subsurface architecture, there is a substantial need for an efficient and reliable methodology to image the results in three dimensions.

Progress in imaging the results in three dimensions was made by combining 1D inversion models into 3D gridded data models (e.g. Lane et al., 2000; Jørgensen et al., 2005; Bosch et al., 2009; Palamara et al., 2010; Jørgensen et al., 2013). However, this integration gave limited consideration to uncertainties related to the interpolation procedure (e.g. Pryet et al., 2011). To minimise these uncertainties different approaches were developed, including an integrated geophysical and geological interpretation based on AEM surveys, reflection seismic sections, borehole data and logs. This provides the most reliable results and leads to a minimisation of interpretational uncertainties (e.g. Gabriel et al., 2003; Jørgensen et al., 2003a; BurVal Working Group, 2009; Jørgensen & Sandersen, 2009; Høyer et al., 2011; Jørgensen et al., 2013). However, little attention has been paid to developing methodologies with an integrated interpretation using different geological and geophysical data sets for the shallow subsurface.

The aim of this paper is to provide a methodology to construct a 3D subsurface model with reduced interpretation uncertainties by integrating AEM, borehole and seismic data. The method was applied and tested with data sets 6 km south from Cuxhaven, northwest Germany. The study area comprises Neogene sediments that are incised by an Elsterian tunnel valley. Previous studies focused on overview mapping of Neogene and Palaeogene marker horizons and Pleistocene tunnel valleys from 2D reflection seismic sections and borehole logs (Gabriel et al., 2003; BurVal Working Group, 2009; Rumpel et al., 2009). Larger conductive structures within the valley fill were identified from 1D inversion results of frequency-domain helicopter-borne electromagnetic data (HFEM) and time-domain helicopter-borne electromagnetic data (HTEM) inversion results (Rumpel et al., 2009; Steuer et al., 2009). Using the previous results and interpretations as well as our new data sets, we provide a detailed analysis of the seismic facies and sedimentary systems included in a 3D geological subsurface model, resolving architectural elements in much greater detail. We generated 3D resistivity grids based on the geostatistical analysis and interpolation of 1D AEM inversion results. The 3D resistivity grids combine the advantage of volumetric computations with the visualisation of wide resistivity ranges and allow the direct comparison and implementation of additional data sets such as borehole and seismic data to improve the geological interpretation of the shallow subsurface.

Geological setting and previous research

The study area is 7.5 km by 7.5 km and is located in northwest Germany, between Cuxhaven in the north and Bremerhaven in the south (Fig. 1A). The study area belongs to the Central European Basin System that evolved from the Variscan foreland basin in the Late Carboniferous (Betz et al., 1987).

In Permian times a wide continental rift system developed, resulting in N-S trending graben structures (Gast & Gundlach, 2006). During the Late Permian, repeated marine transgressions flooded the subbasins and thick evaporite successions formed (Pharaoh et al., 2010). Extensional tectonics during the Middle to Late Triassic led to the formation of NNE-SSW trending graben structures, following the orientation of major basement faults. The main extensional phase in the Late Triassic was accompanied by strong salt tectonics and rim-syncline development (Kockel, 2002; Grassmann et al., 2005; Maystrenko et al., 2005a). During the Late Cretaceous to Early Palaeogene, the area was tectonically reactivated, an event that is related to the Alpine Orogeny (Maystrenko et al., 2005a) and was accompanied by local subsidence and ongoing salt tectonics (Baldschuhn et al., 1996, 2001; Kockel, 2002; Grassmann et al., 2005; Maystrenko et al., 2005a; Rasmussen et al., 2010).

Palaeogene and Neogene marginal-marine deposits

Since the Late Oligocene, sedimentation in the North Sea Basin has been dominated by a large clastic depositional system, fed by the Baltic River System (Huuse & Clausen, 2001; Overeem et al., 2001; Huuse, 2002; Kuster, 2005; Møller et al., 2009; Knox et al., 2010; Anell et al., 2012; Rasmussen & Dybkjær, 2013; Thöle et al., 2014). Initially the Baltic River System, draining the Fennoscandian Shield and the Baltic Platform, prograded from the northeast, and then the sediment transportation direction rotated clockwise to southeast (Sørensen et al., 1997; Michelsen et al., 1998; Huuse et al., 2001).

Early Miocene deposits in the study area consist of fine-grained glauconite-rich marine outer shelf deposits bounded at the base by an unconformity (Gramann & Daniels, 1988; Gramann, 1989; Overeem et al., 2001; Kuster, 2005). K-Ar apparent ages of these sediments range from 24.8 to 22.6 Ma (Odin & Kreuzer, 1988), indicating that the basal unconformity correlates with the marked climatic deterioration and eustatic sea-level fall at the Palaeogene-Neogene transition (Huuse & Clausen, 2001; Zachos et al., 2001; Miller et al., 2005; Rasmussen et al., 2008, 2010; Anell et al., 2012).

The lower boundary of the Middle to Late Miocene deposits is the intra Middle Miocene unconformity. The unconformity can be traced as a strong seismic reflector or as a prominent downlap surface in most parts of the North Sea Basin (Cameron et al., 1993; Michelsen et al., 1995; Huuse & Clausen, 2001; Rasmussen, 2004; Møller et al., 2009; Anell et al., 2012) and coincides with a significant depositional hiatus in the southern,

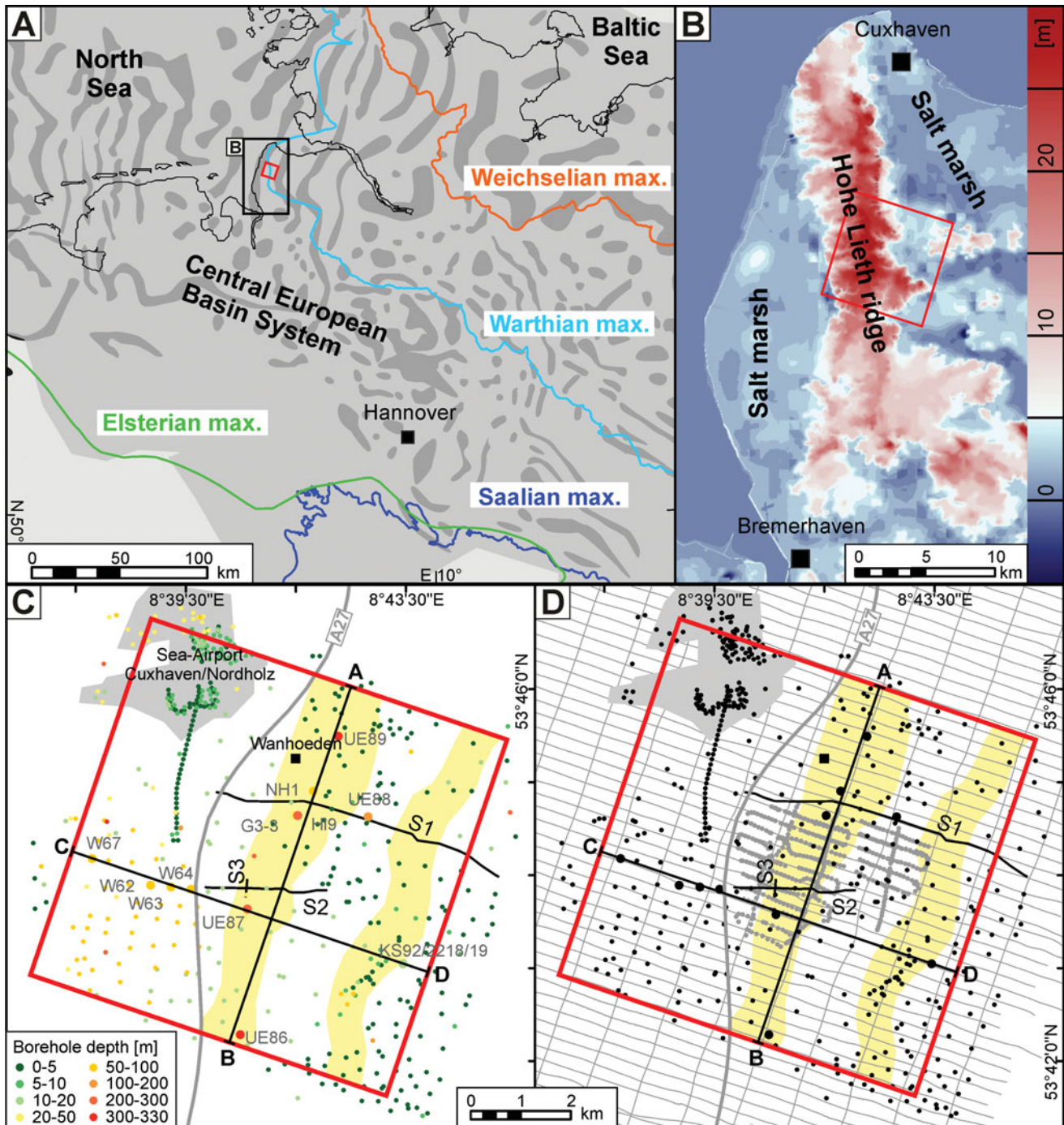


Fig. 1. (A) Location of the study area and maximum extent of the Pleistocene ice sheets (modified after Jaritz, 1987; Baldschuhn et al., 1996, 2001; Scheck-Wenderoth & Lamarche, 2005; Ehlers et al., 2011). (B) Hill-shaded relief model of the study area, showing the outline of the Hohe Lieth ridge. (C) Close-up view of the study area showing the location of Pleistocene tunnel valleys (light yellow) and the location of boreholes (coloured dots). Boreholes used in the seismic and cross-sections are indicated by larger dots; seismic sections S1 (Fig. 4), S2 and S3 (Fig. 5) are displayed as black lines. Cross-section A–B is visualised in Fig. 6; C–D is visualised in Fig. 7. (D) HFEM surveys are displayed as grey lines; HTEM surveys are displayed as dark grey dots.

central and northern North Sea Basin (Rundberg & Smalley, 1989; Huuse & Clausen, 2001; Stoker et al., 2005a,b; Eidvin & Rundberg, 2007; Köthe, 2007; Anell et al., 2012).

The Middle Miocene hiatus is characterised by sediment starvation and/or condensation, and might have resulted from

a relative sea-level rise, either eustatic or in combination with tectonic subsidence (Gramann & Kockel, 1988; Cameron et al., 1993; Anell et al., 2012). In the study area the age of the Middle Miocene unconformity is dated to 13.2–14.8 Ma (Köthe et al., 2008). The overlying fine-grained, glauconite-rich

Middle Miocene shelf deposits are characterised by an overall fining-upward trend (Gramann & Daniels, 1988; Gramann, 1989; Overeem et al., 2001; Kuster, 2005).

The Middle Miocene climatic optimum corresponds to a sea-level highstand, which was followed by a climatic cooling and an associated sea-level fall during the late Middle Miocene (Haq et al., 1987; Jürgens, 1996; Zachos et al., 2001; Kuster, 2005; Miller et al., 2005). In the study area, Late Miocene deposits consist of shelf and storm-dominated shoreface deposits with an overall coarsening-upward trend (Gramann & Kockel, 1988; Gramann, 1988, 1989; Kuster, 2005) and K–Ar apparent ages ranging between 9.5 and 11 Ma (Odin & Kreuzer, 1988).

The Pliocene was characterised by several cycles of transgression and regression, resulting in the formation of unconformities, which can be traced in most areas of the North Sea Basin (Mangerud et al., 1996; Konradi, 2005; Kuhlmann & Wong, 2008; Thöle et al., 2014).

Pleistocene deposits

The Early Pleistocene was characterised by marine to fluvio-deltaic sedimentation in the study area (Gibbard, 1988; Kuhlmann et al., 2004; Streif, 2004). Subsequently, the Middle Pleistocene (MIS 12 to MIS 6) Elsterian and Saalian ice sheets completely covered the study area (Fig. 1A); the Late Pleistocene Weichselian glaciation did not reach the study area (e.g. Caspers et al., 1995; Streif, 2004; Ehlers et al., 2011; Roskosch et al., 2014).

During the Elsterian glaciation, deep tunnel valleys were subglacially incised into the Neogene and Pleistocene deposits of northern Central Europe (Huuse & Lykke-Andersen, 2000; Lutz et al., 2009; Stackebrandt, 2009; Lang et al., 2012; van der Vegt et al., 2012; Janszen et al., 2012, 2013). In this period, the 0.8–2 km wide and up to 350 m deep Cuxhaven tunnel valley formed (Kuster & Meyer, 1979; Ortlam, 2001; Wiederhold et al., 2005a; Rumpel et al., 2009). The valley is filled with Elsterian meltwater deposits and till (Gabriel, 2006; Rumpel et al., 2009), overlain by the Late Elsterian glaciolacustrine Lauenburg Clay Complex and marine Holsteinian interglacial deposits, which consist of interbedded sand and clay (Kuster & Meyer, 1979, 1995; Linke, 1993; Knudsen, 1988, 1993a,b; Müller & Höfle, 1994; Litt et al., 2007). 2D resistivity sections based on AEM surveys indicate that depositional units of the valley fill can vary in thickness over a short distance (Siemon et al., 2002; Gabriel et al., 2003; Siemon, 2005; Rumpel et al., 2009; Steuer et al., 2009; BurVal Working Group, 2009). The Elsterian and interglacial Holsteinian deposits of the tunnel-valley fill and the adjacent Neogene host sediments are overlain by Saalian sandy meltwater deposits and till (Kuster & Meyer, 1979; Ehlers, 2011). The morphology of the study area is characterised by an up to 30 m high Saalian terminal moraine complex, the Hohe Lieth ridge (Fig. 1B; Ehlers et al., 1984). Eemian tidal salt marsh deposits together with Holocene fluvial deposits, peats and soils

characterise the lowland on both sides of the Hohe Lieth ridge (Fig. 1B; Höfle et al., 1985; Binot & Wonik, 2005; Panteleit & Hammerich, 2005; Siemon, 2005).

Database

The database includes 488 borehole logs, three 2D reflection seismic sections and two AEM surveys, comprising both HFEM and HTEM data (Fig. 1C and D). Most of the data sets were acquired between 2000 and 2005 by the BurVal project (Blindow & Balke, 2005; Wiederhold et al., 2005a,b; BurVal Working Group, 2009; Tezkan et al., 2009).

Borehole data and geological depth maps

Paradigm™ GOCAD® software (Paradigm, 2011) was used to construct an initial 3D geological subsurface model from a Digital Elevation Model (DEM) with a resolution of 50 m and published depth maps of the Cenozoic succession (Baldschuhn et al., 1996; Rumpel et al., 2009; Hese, 2012). Lithology logs of 488 boreholes were used to analyse the subsurface architecture of the Cenozoic deposits and to define major geological units. The commercial software package GeODin® (Fugro Consult GmbH, 2012) was used for the data management.

Borehole location data were corrected for georeferencing errors. The interpretation of the tunnel-valley fill is based on five borehole logs penetrating all five lithologic facies units (Fig. 1C). A resistivity log was only available for borehole HL9 Wanhoeden located in the centre of our test site, penetrating the Cuxhaven tunnel valley (Fig. 1C).

Seismic sections

The seismic surveys were acquired by the Leibniz Institute for Applied Geophysics Hannover (LIAG, formerly the GGA Institute) in 2002 and 2005. The three 2D reflection seismic sections were used to map the large-scale subsurface architecture of the study area (black lines in Fig. 1C). The 2D reflection seismic sections include a 6 km long WNW–ESE oriented seismic line S1 and a 2.4 km long W–E trending seismic line S2 that is located 1 km further to the south (Fig. 1C). Seismic line S2 intersects with the 0.4 km long, N–S trending seismic line S3. The survey design and the processing of the seismic sections, lines S1 (Wanhoeden), S2 (Midlum 3) and S3 (Midlum 5), are described by Gabriel et al. (2003), Wiederhold et al. (2005b) and Rumpel et al. (2006a,b; 2009).

Data processing was carried out using ProMax® Landmark software. Processing followed the workflow for vibroseis data described by Yilmaz (2001). The seismic vibrator operated with a sweep ranging from 50 to 200 Hz. The survey design led to a maximum target depth of 1600 m with a common-midpoint spacing of 5 m for seismic line S1 and 2.5 m for seismic lines

S2 and S3. Assuming a velocity of 1600 m/s and a maximum frequency of about 150 Hz, wavelengths of about 10 m are expected and thus the minimum vertical resolution should be in the range of a quarter of a wavelength but at least about 4 m for the shallow subsurface. Increasing velocity and decreasing frequency with depth leads to a decrease in resolution with depth (wavelength of about 22 m in 1000 m depth). For migration as well as for depth conversion a simple smooth velocity function is used with a start velocity of 1500 m/s increasing to about 2200 m/s at 1000 m depth.

Acquisition, processing and visualisation of AEM data

Frequency-domain helicopter-borne electromagnetics The HFEM survey covering the entire study area (Fig. 1D) was conducted by the Federal Institute for Geosciences and Natural Resources (BGR) in 2000. The survey grid consisted of parallel WNW–ESE flight lines with an average NNE–SSW spacing of 250 m, connected by tie lines perpendicular to the flight lines with a WNW–ESE spacing of 1000 m (grey lines in Fig. 1D). The distance between consecutive values was 3–4 m, assuming an average flight velocity of about 140 km/h during the survey (Siemon et al., 2004). The HFEM system comprised a five-frequency device (Siemon et al., 2002). The transmitter/receiver coil configuration was horizontal co-planar for all frequencies. The transmitter coils operated at frequencies of 0.4 kHz, 1.8 kHz, 8.6 kHz, 41.3 kHz and 192.6 kHz (Siemon et al., 2004). The maximum penetration depth was about 150 m, depending on the subsurface resistivity distribution. The sampling rate was 0.1 s and the signal was split into its in-phase I and out-of-phase Q components relative to the transmitter signal. Because of the relatively small system footprint (about 100–150 m), i.e. the lateral extent of the main inductive response beneath the system, the data set is characterised by a rather high spatial resolution, which decreases with depth (Siemon et al., 2004). The inversion of HFEM data to resistivity and depth values followed the workflow developed in Sengpiel & Siemon (2000) and Siemon (2001). It depended on an initially unknown subsurface resistivity distribution. Initially the resistivity was calculated based on a half-space model (Fraser, 1978). If the resistivity varies with depth, the uniform half-space model will yield different ‘apparent resistivity’ and ‘apparent distance’ values at each HFEM frequency (Siemon, 2001). The centroid depth is a measure for the penetration of the electromagnetic fields and represents the centre of the half-space. This depth value depends on the individual HFEM frequencies and on the resistivity distribution in the subsurface: the higher the ratio of resistivity and frequency, the greater the centroid depth. The apparent resistivity and centroid depth data pairs were used to determine a set of sounding curves at each data point. The apparent resistivity vs centroid depth-sounding curves are a smooth approximation of the vertical resistivity distribution

and were also used to define an individual six-layer starting model at each data point for an iterative Marquardt–Levenberg inversion. The model parameters were modified until a satisfactory fit between the survey data and the calculated field data from the inversion model was achieved (Sengpiel & Siemon, 2000; Siemon et al., 2009a,b). Based on the low number of input parameters available (two per frequency), which can be resolved by 1D inversion, the number of individual model layers is limited. The 1D HFEM inversion results were extracted as a set of data points (reduced to approximately one sounding or 1D model every 7 m along the flight lines). The apparent resistivities are displayed separately at each frequency.

Time-domain helicopter-borne electromagnetics An HTEM survey was conducted by the University of Aarhus (BurVal Working Group, 2009; Rumpel et al., 2009) on behalf of the Leibniz Institute for Applied Geophysics (LIAG, formerly the GGA Institute). The HTEM soundings are restricted to an area of about 3.96 km by 2.8 km (grey dots in Fig. 1D). The HTEM system operated with a transmitter loop on a six-sided frame (Sørensen & Auken, 2004). In the Cuxhaven survey, the distance between consecutive soundings was about 75 m, assuming an average flight velocity of 18 km/h during the survey (Fig. 1D).

The system operated with low and high transmitter moments. A low transmitter moment of approximately 9000 Am² was generated by a current of 40 A in one measurement cycle. The received voltage data were recorded in the time intervals between 17 and 1400 μs. A current of 40–50 A in four loop turns generated a high moment of approximately 47,000 Am². The voltage data of high moment measurements were recorded in the time interval of 150–3000 μs. Acquisition for both the low and high transmitting moments were carried out in cycles for the four data sets (320 stacks per data set for low and 192 stacks per data set for high moment measurement). Subsequently, the arithmetic mean values of the low and high moments were averaged for each of the data sets to generate one data set. This merged data set was interpreted as one geophysical model. The resolution of the uppermost part of the subsurface is limited by the recording lag time of the HTEM system, which does not start until about 17 μs, and strongly depends on the near surface conductivity and thus on lithology and the pore water content (Steuer et al., 2009). This results in near-surface layers being commonly merged into one layer in the model.

The maximum penetration depth is about 250 m and depends on the subsurface resistivity. Because the method cannot resolve thin depositional units (<5 m), individual depositional units may be merged into thicker model layers. With increasing depth the resolution decreases, thus restricting the vertical resolution to approximately 15–20 m in the shallow subsurface and decreasing to 20–50 m at 100 m depth. The horizontal resolution capability also decreases with depth. At about 25 m depth, the diameter of the footprint from which data are obtained is

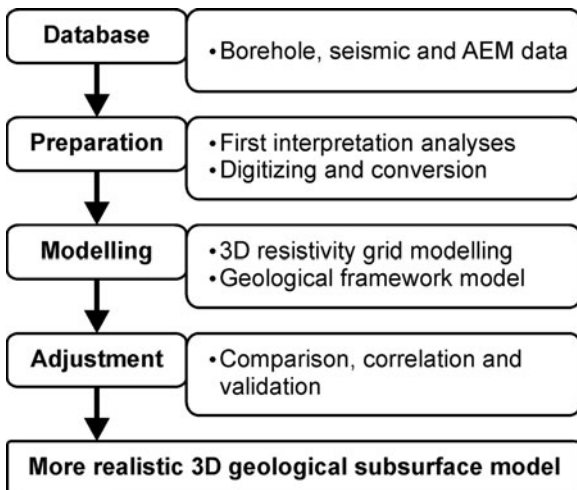


Fig. 2. Workflow.

about 75–100 m and it exceeds 300–400 m at 100 m depth (West & Macnae, 1991; Jørgensen et al., 2005, 2013). Small-scale spatial variations in geology are therefore less well resolved at deeper levels than at shallower levels (Newman et al., 1986).

Aarhus Workbench software was used to process the HTEM data (Steuer, 2008; Steuer et al., 2009). This software integrates all steps in the processing workflow from management of the raw data to the final visualisation of the inversion results. The software provides different filtering and averaging tools, including the correction of GPS signal, tilt and altitude values. HTEM data were inverted with a five-layer model using a spatially constrained inversion (SCI) option of em1divn (Steuer, 2008; Viezzoli et al., 2008; Steuer et al., 2009; HGG, 2011). SCI takes many adjacent data sets into account, which are connected by distant dependent lateral constraints to impose continuity in areas with sparser data coverage. The lateral constraints were defined by the expected geological continuity of each layer. The inversion results strongly depended on the starting model used and the SCI settings, especially the strength of constraints.

The 1D HTEM inversion results were extracted as a set of models, which were characterised by a limited spatial resolution due to the large distance between soundings and the relatively large lateral extent of the main inductive response beneath the system.

Methodology of combined geological and geophysical analysis

To improve the interpretation of the subsurface architecture we developed a workflow in which the interpretation results of borehole lithology logs, 2D reflection seismic sections and 3D resistivity grids based on 1D AEM inversion results were integrated (Figs 2 and 3). In order to achieve this we

used Paradigm™ GOCAD® software for 3D subsurface modelling (Paradigm, 2011).

Construction of an initial 3D geological subsurface model based on the interpretation of borehole and seismic data

In the first step a basic subsurface model of the Cuxhaven tunnel valley and its Neogene host sediments was constructed by integrating borehole lithology logs and 2D reflection seismic sections (Tables 1 and 2; Figs 3A and 4–7). For the analysis of seismic sections we used the scheme of Mitchum et al. (1977). Each seismic unit is defined by the external geometry, the internal reflector configuration and seismic facies parameters, such as amplitude, continuity and density of reflectors (Tables 1 and 2; Figs 4 and 5). The 2D seismic interpretation results combined with borehole lithology analysis defined 15 stratigraphic marker horizons, which represent the tops of each depositional unit (Tables 1 and 2).

In GOCAD we applied a discrete modelling approach that creates triangulated surfaces from points, lines, and open and closed curves (Mallet, 2002). With the Discrete Smooth Interpolation (DSI) algorithm the roughness of the triangulated surfaces was minimised (Mallet, 2002). The 3D subsurface model consists of a series of triangulated surfaces representing the bounding surfaces of the depositional units (cf. Tables 1 and 2; Fig. 3).

Construction of 3D resistivity grids based on AEM data

The best technique to transform subsurface resistivity data from a set of 1D vertical inversion models into a 3D model is 3D interpolation. The applied 3D interpolation algorithm requires discrete data in all directions, discarding the layered approach used in the inversion, and leads to a smoothing effect between previously defined layer boundaries of 1D AEM inversion.

In the first step, the 1D AEM inversion models were imported into the GOCAD modelling software (Fig. 3B). Subsequently, each AEM data set was transformed in a regular spaced voxel grid with rectangular hexahedral cells.

The large differences in AEM data distribution and penetration depths required the construction of two independent grid models with different resolutions. For the data set of 1D HFEM inversion results we choose a grid with horizontal and vertical cell sizes of 10 m and 1 m, respectively, which provides a good compromise between data resolution and model handling. For the data set of 1D HTEM inversion results an enlarged grid with horizontal and vertical cell sizes of 20 m and 2.5 m, respectively, provides the best results.

The arithmetic mean was used to transform and estimate the resistivity value of a cell based on each 1D AEM inversion model. The estimation of resistivity at unsampled locations to

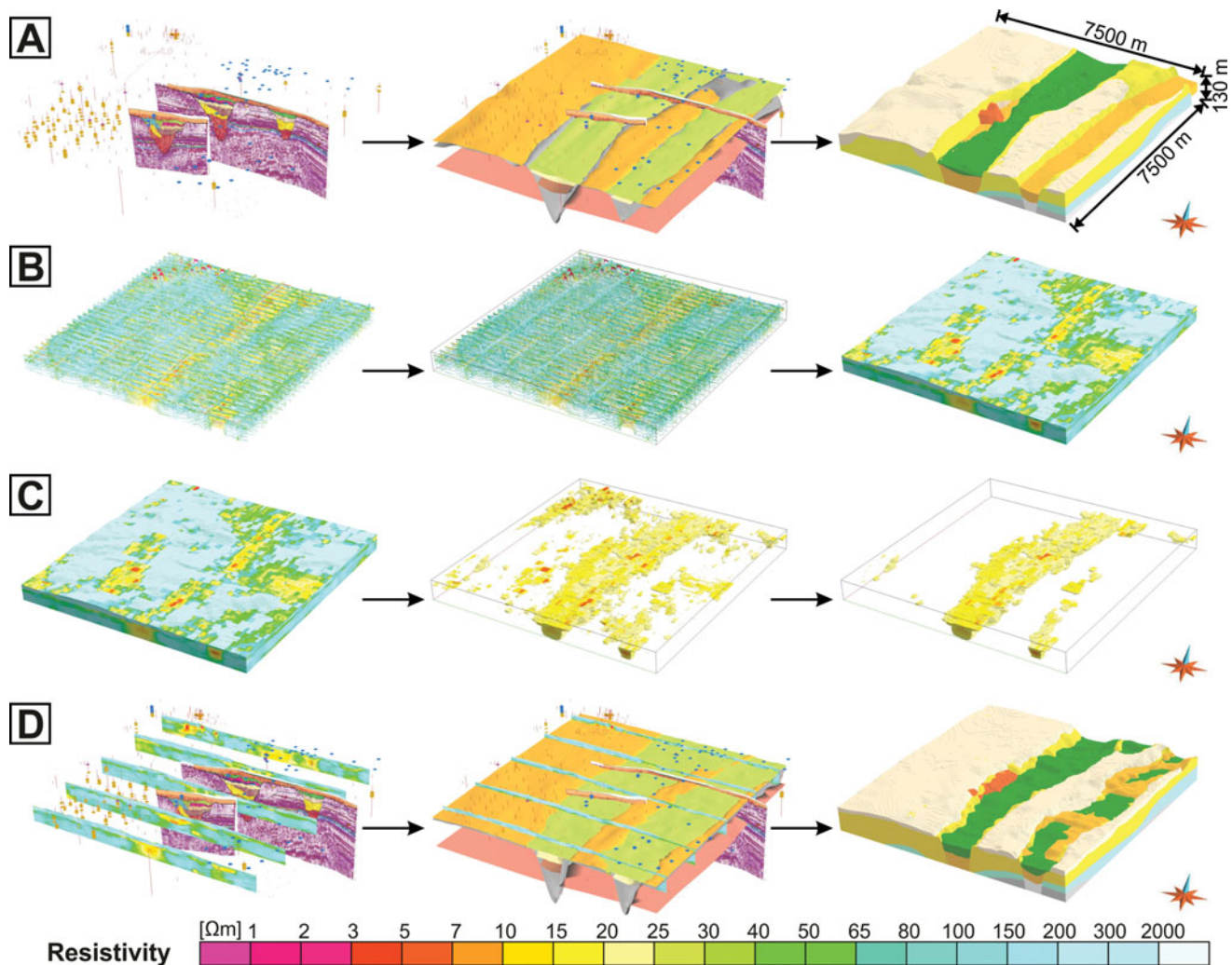


Fig. 3. Workflow of the construction of combined geological/geophysical subsurface models, illustrated by HFEM data. (A) Construction of the 3D geological subsurface model based on borehole and seismic data. (B) Construction of a continuous 3D resistivity voxel grid based on 1D HFEM inversion results. The resistivity data were integrated into a regular structured grid, analysed by means of geostatistical methods and subsequently interpolated. (C) The selection of specific resistivity ranges provides a first estimate of the large-scale depositional architecture. Shown is the clay distribution in the study area, indicated by HFEM resistivity values between 3 and 25 Ωm . (D) Adjustment of the 3D geological subsurface model by integrating information of the 3D resistivity grid.

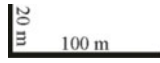
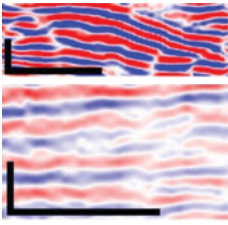
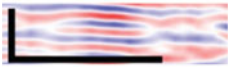
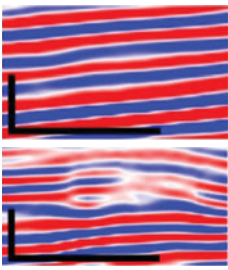
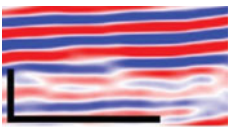
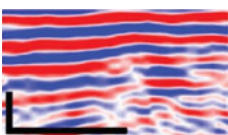
get a continuous 3D resistivity grid model of the subsurface was achieved by the ordinary kriging method (Krige, 1951). A 1D vertical analysis combined with a 2D horizontal analysis of the 1D AEM inversion models was carried out since sedimentary successions tend to be more variable in the vertical than in the horizontal direction and this often results in zonal anisotropy. Kriging uses semivariogram models to infer the weighting given to each data point and therefore takes both distance and direction into account. Variography was performed in different directions (azimuths of 0° , 45° , 90° and 135°) with a tolerance of 22.5° and an adjusted bandwidth to survey the resistivity isotropy in each resistivity model (Fig. 8). For each AEM data set, best results in block weighting were obtained by using an exponential function. The analysis of HFEM data results in a vertical range of 25 m and a horizontal major principal axis

with an angle of 19° and a range of 1000 m, and a perpendicular minor principal axes with a range of 780 m (Fig. 8). The analysis of HTEM data results in a vertical range of 50 m and a horizontal major principal axes with an angle of 130° and a range of 1500 m, and a perpendicular minor principal axes with a range of 1300 m (Fig. 8). The 3D interpolation results for each voxel over the whole study area in an estimated value for the resistivity.

Uncertainties of 3D resistivity grid modelling

1) Data processing of vintage 1D AEM inversion models did not focus on the elimination of anthropogenic effects (such as the airport Cuxhaven/Nordholz in the northwest of the study area). Hence, the processed AEM databases contained

Table 1. Seismic and sedimentary facies of the Oligocene and Neogene marine to marginal marine deposits

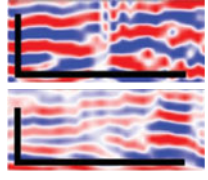
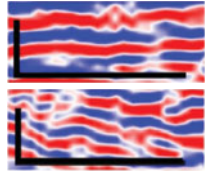
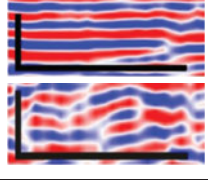
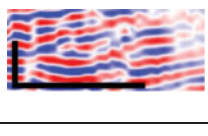
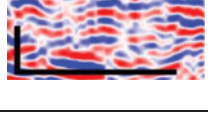
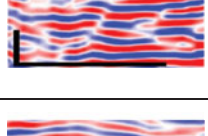
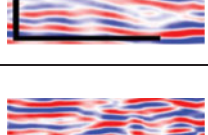
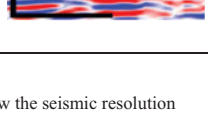
	Seismic pattern		Sedimentary facies	Interpretation	Seismic unit	Thick-ness (m)	ρ (Ωm)				
							B + S	AEM	Lith.		
Pliocene	Hummocky, high-amplitude reflectors and sub-parallel, partly hummocky and U-shaped, low-amplitude and transparent reflectors		Fine sand and silt	Estuarine deposits (Gramann, 1989; Kuster, 2005) of an incised valley	U4	30–120	99	97	100		
Miocene	Late	Mess.	Sub-parallel, partly hummocky, low-amplitude reflectors		Fine sand	Open shelf to storm-dominated deposits of the upper and lower shoreface (Gramann, 1989; Rasmussen et al., 2010; Rasmussen & Dybkjær, 2013)	U3	15–40	88	90	100
		Tort.	Continuous, sub-parallel, partly hummocky, high-amplitude reflectors		Clay and silt coarsening upwards into fine sand			30–85	73	75	40
	Middle	Serra.	Continuous, parallel, partly hummocky, high-amplitude reflectors		Glauconitic clay and silt	Transgressive shelf deposits (Gramann, 1989; Kuster, 2005; Köthe, 2008; Rasmussen et al., 2010)	U2	10–70	–	–	–
		Lang.	Continuous, sub-horizontal, parallel, partly hummocky, high-amplitude reflectors		Glauconitic clay, silt and fine sand	Marine outer shelf deposits (Gramann, 1989; Overeem et al., 2001; Kuster, 2005)	U1	10–85	–	–	–
	Early	Burg.	Continuous, sub-horizontal, parallel, partly hummocky, high-amplitude reflectors		Glauconitic clay, silt and fine sand	Marine outer shelf deposits (Gramann, 1989; Overeem et al., 2001; Kuster, 2005)	U1	10–85	–	–	–
Oligocene	Continuous, sub-horizontal, high-amplitude reflectors and discontinuous, partly inclined, low-amplitude reflectors, partly transparent		Clay, silt and fine sand	Marine deposits (Gramann, 1989; Kuster, 2005)	U0	~220	–	–	–		

Median resistivity values are extracted from the HFEM grid model and are related to the 3D geological subsurface model based on borehole and seismic data (B + S), the adjusted 3D geological subsurface model derived from the 3D AEM resistivity grids (AEM) and the adjusted 3D geological subsurface model with manually adjusted resistivity values based on lithology log information (Lith.).

- erroneous data from anthropogenic noise (Siemon et al., 2011).
- 2) 1D AEM inversion models are always simplified realisations of the subsurface resistivity distribution, particularly if only models with few layers are used to explain the AEM data. As AEM resolution capability decreases with depth, the

- layer thicknesses generally increase with depth, which corresponds to the probability that several thin layers of various depositional units may be merged to a thicker resistivity layer.
- 3) Uncertainties may originate from the interpolation method (Pryet et al., 2011). We focused on uncertainties caused by

Table 2. Seismic and sedimentary facies of the Pleistocene deposits

		Seismic pattern	Sedimentary facies	Interpretation	Seismic unit	Thickness (m)	ρ (Ω m)				
							B + S	AEM	Lith.		
Holocene											
Pleistocene	Late	Wei.	Thickness is below the seismic resolution	Fine sand and peat, contain clay and silt	Salt marsh deposits (Höfle et al., 1985; Knudsen, 1988; Gabriel, 2006)	up to 9	64	64	60		
	Eem.										
	Saalian	Drenthe	Hummocky, low- to high-amplitude reflectors passing laterally into continuous, horizontal-parallel or parallel-inclined reflectors		Fine to coarse sand and diamicton	Diamicton, glaciofluvial and terminal moraine deposits (Ehlers, 2011)	U5.8 sat. unsat.	10–50	128	138 480	140 500
		Holsteinian	Discontinuous, hummocky to inclined-parallel, high- to medium-amplitude reflectors		Clay, silt and fine sand with shells	Marine to marginal marine deposits (Kuster & Meyer, 1979; Knudsen, 1988)	U5.7 U5.7*	6–45	24 69	32	30
	Middle	Elsterian	Horizontal-parallel reflectors passing laterally into discontinuous, hummocky high- to medium-amplitude reflectors		Clay and silt with some fine sand	Glaciolacustrine deposits of the Upper Lauenburg Clay Complex (Kuster & Meyer, 1979)	U5.6 U5.6*	10–45	16	14 52	10 10
			Continuous to discontinuous, hummocky, parallel, medium- to high-amplitude reflectors		Fine to medium sand, silty	Glaciolacustrine deposits of the Lower Lauenburg Clay Complex (Kuster & Meyer, 1979)	U5.5 U5.5*	20–35	29 100	25 91	25 70
			Discontinuous, hummocky, low- to high-amplitude reflectors		Fine to medium sand, delta deposit	Glaciolacustrine deposits of the Lower Lauenburg Clay Complex (Kuster & Meyer, 1979; Ortlam, 2001)	U5.4	up to 50	33	34	150
			Discontinuous, parallel, hummocky, medium- to low-amplitude reflectors, partly transparent		Clay and silt	Glaciolacustrine deposits of the Lower Lauenburg Clay Complex (Kuster & Meyer, 1979)	U5.3	up to 55	31	27	15
			Parallel-inclined, hummocky, subhorizontal, low- to high-amplitude reflectors		Fine sand fining upwards to silty clay	Fine-grained glaciofluvial deposits (Kuster & Meyer, 1979)	U5.2 U5.2*	25–65	38 66	35 58	35 35
			Discontinuous, partly inclined and hummocky, high- to medium-amplitude reflectors		Coarse sand and gravel fining upwards into medium sand	Coarse-grained glaciofluvial deposits, basal tunnel-valley fill (Kuster & Meyer, 1979)	U5.1	70–160	41	33	120
Thickness is below the seismic resolution				Fine to medium sand, silt, pebbles	Proglacial meltwater deposits		up to 10	67	66	70	

Median resistivity values are extracted from the HFEM grid model and are related to the 3D geological subsurface model based on borehole and seismic data (B + S), the adjusted 3D geological subsurface model derived from the 3D AEM resistivity grids (AEM) and the adjusted 3D geological subsurface model with manually adjusted resistivity values based on lithology log information (Lith.). Seismic subunits U5.1–U5.8 refer to the Cuxhaven tunnel-valley fill. Values marked with * refer to the small-scale tunnel valley east of the Cuxhaven tunnel valley.

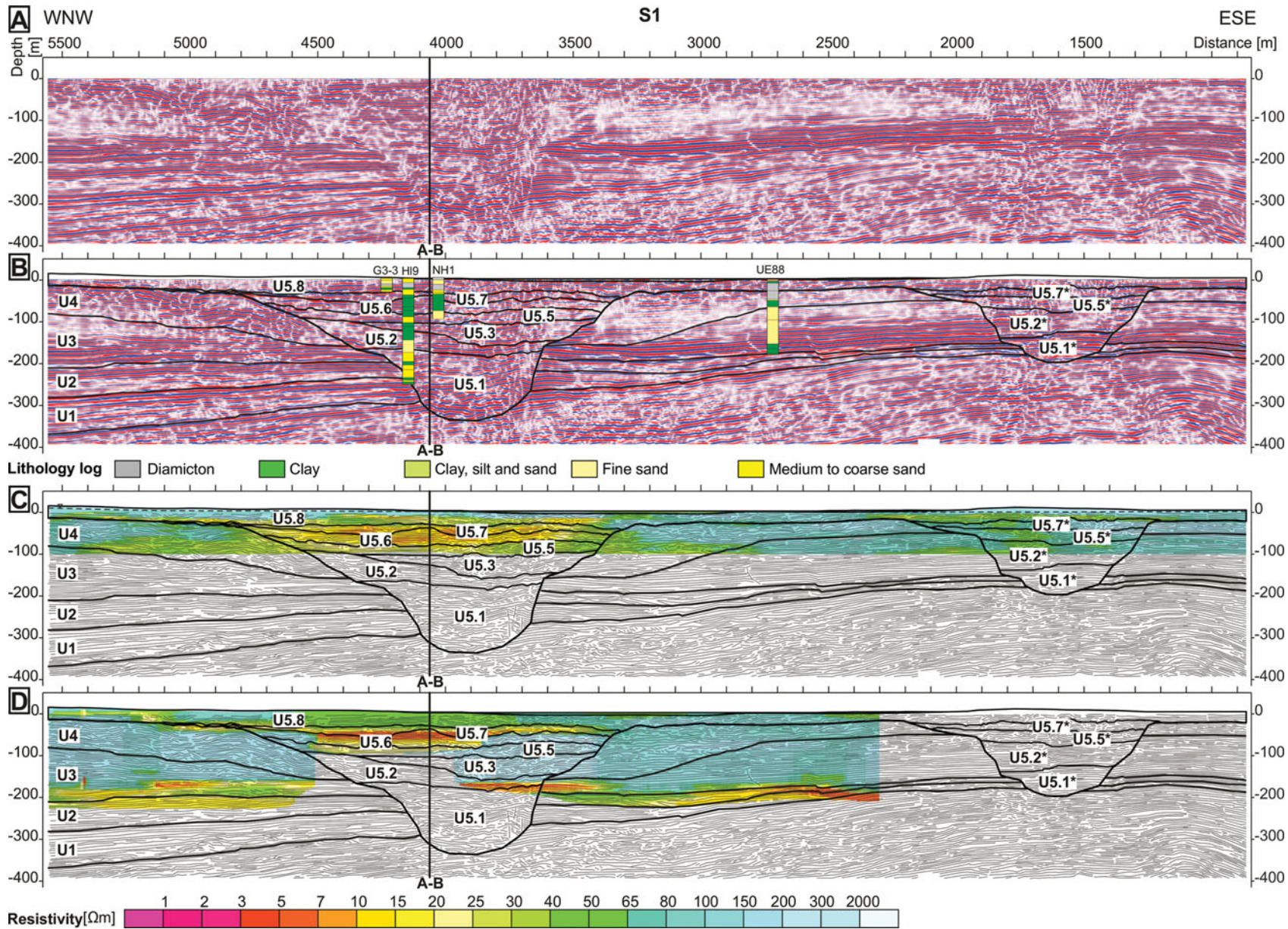


Fig. 4. 2D reflection seismic section S1 combined with airborne electromagnetic data. (A) 2D reflection seismic section S1. (B) Interpreted seismic section S1 with borehole logs. Seismic units are described in Tables 1 and 2. (C) 2D reflection seismic section S1 combined with resistivity data, extracted from the 3D HFEM resistivity grid. The dashed line indicates the groundwater table. (D) 2D reflection seismic section S1 combined with resistivity data, extracted from the 3D HTEM resistivity grid. For location see Fig. 1C and D.

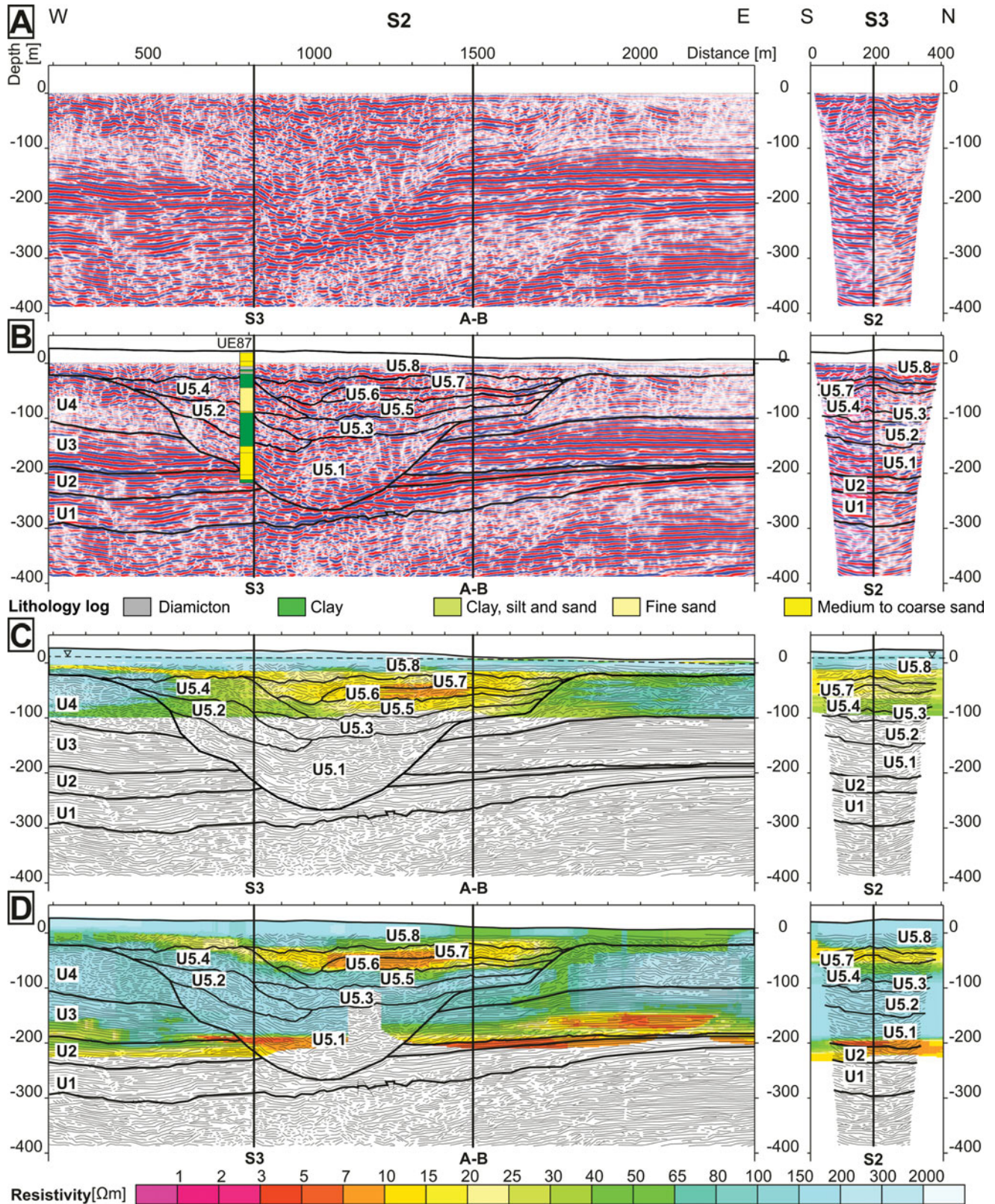


Fig. 5. 2D reflection seismic sections S2 and S3 combined with airborne electromagnetic data. (A) 2D reflection seismic sections S2 and S3. (B) Interpreted seismic sections S2 and S3 with borehole logs. Seismic units are described in Tables 1 and 2. (C) 2D reflection seismic sections S2 and S3 combined with resistivity data, extracted from the 3D HFEM resistivity grid. The dashed line indicates the groundwater table. (D) 2D reflection seismic sections S2 and S3 combined with resistivity data, extracted from the 3D HTEM resistivity grid. For location see Fig. 1C and D.

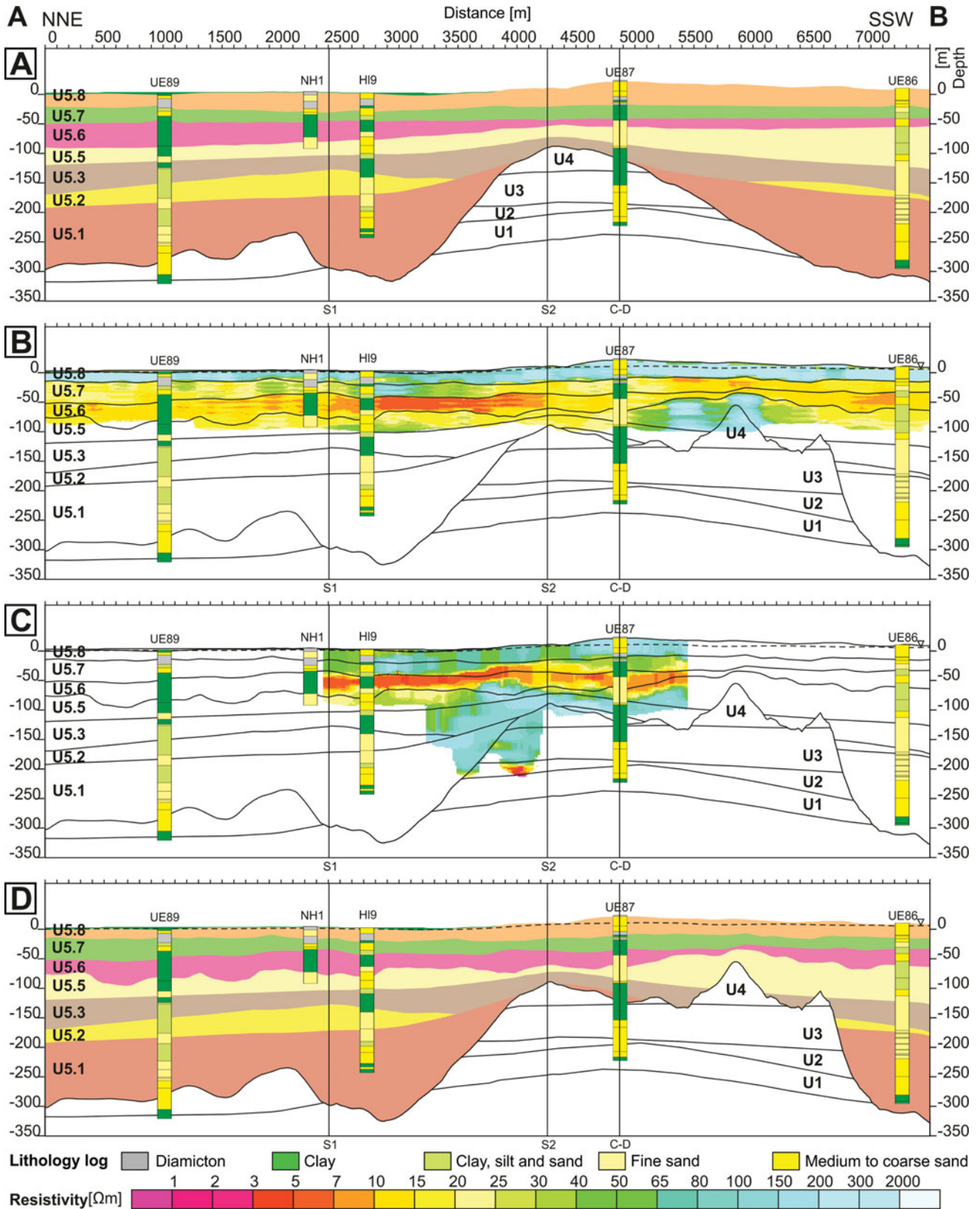


Fig. 6. 2D cross-section of the study area (A–B in Fig. 1C and D), showing major bounding surfaces and resistivity values based on borehole, seismic and AEM data. The dashed line indicates the groundwater table. (A) 2D cross-section extracted from the 3D geological model based on borehole and seismic data. Only the Pleistocene deposits are shown in colour. (B) 2D cross-section extracted from the adjusted 3D geological model and the corresponding resistivities derived from the 3D HFEM voxel grid. (C) 2D cross-section extracted from the adjusted 3D geological model and the corresponding resistivities derived from the 3D HTEM voxel grid. (D) 2D cross-section extracted from the adjusted 3D geological model. Only the Pleistocene deposits are shown in colour.

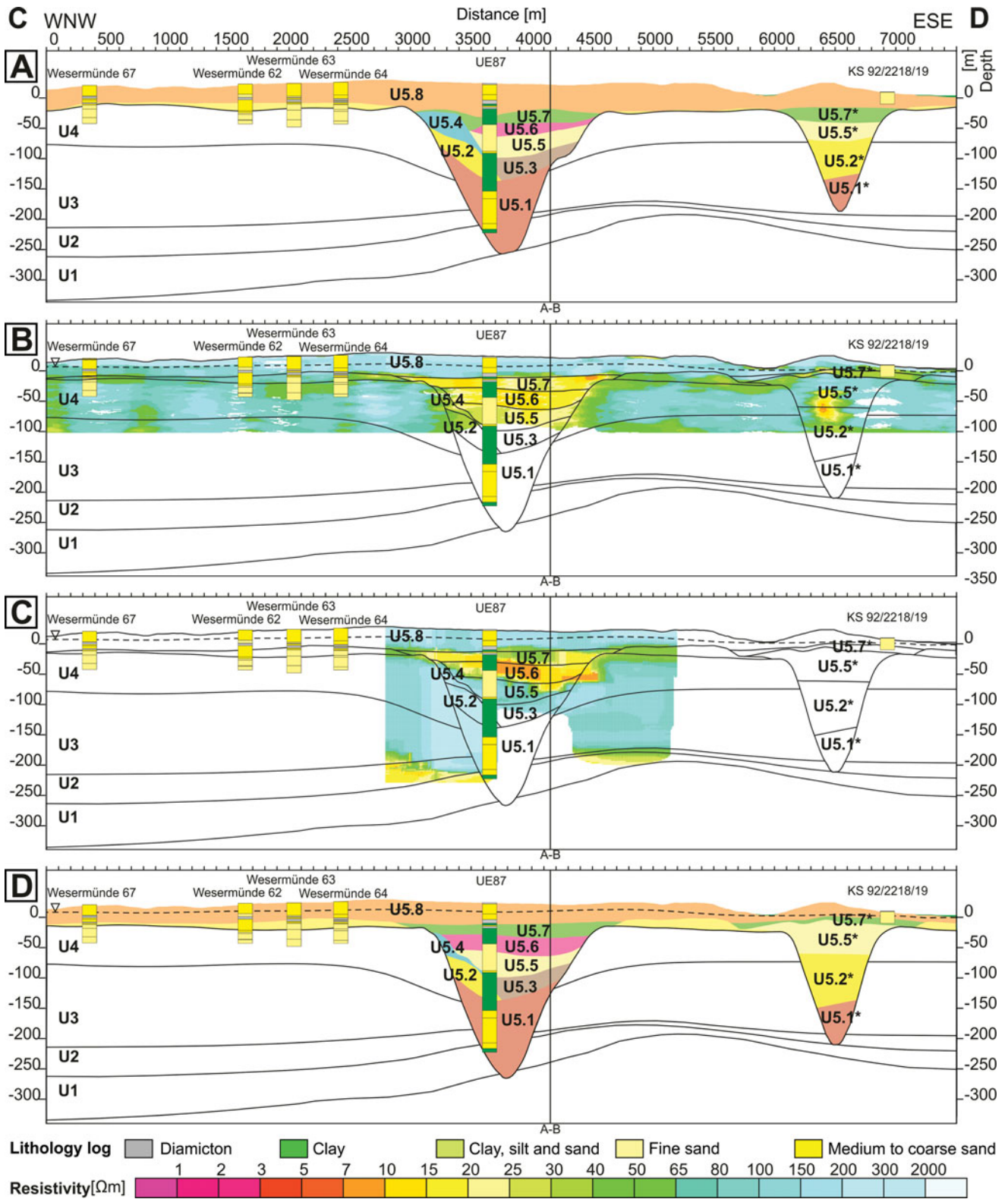


Fig. 7. 2D cross-section of the study area (C–D in Fig. 1C and D), showing major bounding surfaces and resistivity values based on borehole, seismic and AEM data. The dashed line indicates the groundwater table. (A) 2D cross-section extracted from the 3D geological model based on borehole and seismic data. Only the Pleistocene deposits are shown in colour. (B) 2D cross-section extracted from the adjusted 3D geological model and the corresponding resistivities derived from the 3D HFEM voxel grid. (C) 2D cross-section extracted from the adjusted 3D geological model and the corresponding resistivities derived from the 3D HTEM voxel grid. (D) 2D cross-section extracted from the adjusted 3D geological model. Only the Pleistocene deposits are shown in colour.

the kriging interpolation method of the 1D AEM inversion results. A geostatistical uncertainty estimate is provided by the kriging variance $\sigma^2_{KRI}(x, y, z)$, which depends on the spatial variability of the parameter and the distance to individual data points. This leads to the construction of a 3D grid that contains both resistivity values and their uncertainties (Pryet et al., 2011). Once the model is built, the analysis of uncertainties between data points (i.e. between flight lines) is expressed by the standard deviation σ_{KRI} (Fig. 9). The standard deviation can be used to evaluate the credibility of the interpolated data and to eventually exclude soundings or groups of soundings with high uncertainty and instead emphasise high-quality soundings. A value close to zero indicates high probability and a value close to one indicates low probability of resistivity values. This information can be used to evaluate the relationship between borehole lithology and 3D resistivity data and hence to quantify uncertainties in the depositional architecture.

Relationship between lithology and resistivity

Borehole lithology and AEM resistivity were linked with the aim of using resistivity as a proxy for lithology (see: Bosch et al., 2009; Burschil et al., 2012b). The resistivity log from borehole HL9 (Fig. 10) and sediment descriptions from 487 borehole logs (Fig. 1C) were used to combine these parameters (Fig. 11).

The electrical resistivity of sediments is mainly controlled by the presence of clay minerals, the degree of water saturation and the pore water ion content. According to Archie (1942), resistivity for clay-free sediments is inversely proportional to the pore water ion content. If the specific pore water ion content is known throughout the different geological layers and structures, estimates in lithology variations related to the clay content and type can be obtained. Because saline groundwater is absent in the study area, at least at depths resolved by HFEM (Siemon, 2005), resistivity changes are related to changes in lithology.

The lithologies were divided into seven grain-size classes based on the borehole descriptions. In accordance with data resolution, we determined the representative lithology in each borehole and extracted the corresponding interpolated resistivity at this location from the 3D resistivity grids based on the two different AEM data sets. We accept in this step that the lithology logs within the study area have varying resolutions ranging from 1 cm to 1 m, depending on the drilling method and data collection. This may lead to a discrepancy between the lithology log and the vertical resolution of the 3D AEM resistivity grids, resulting in insufficient resistivity–grain size relationships. To reduce the uncertainty between the lithology logs and resistivity grid we analysed all logs and calculated mean and median resistivity values for each class that allowed derivation of grain size from resistivity (Fig. 11). Grouping the data into resistivity classes and counting the number of occurrences of each lithol-

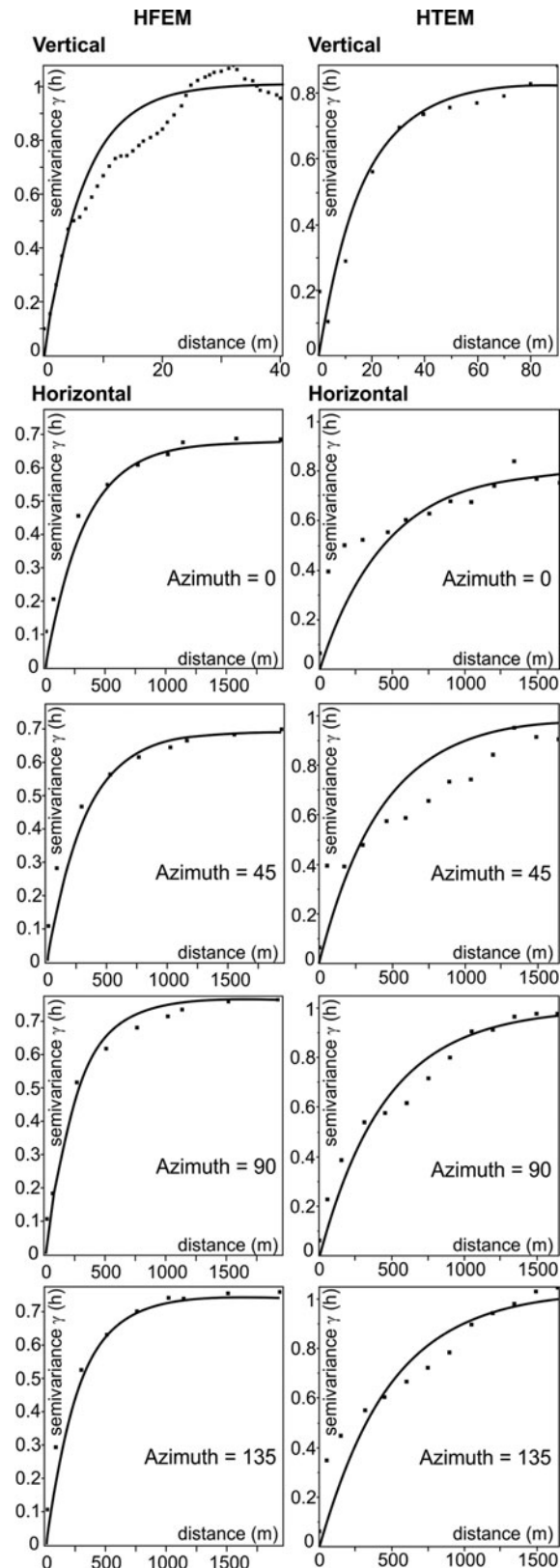


Fig. 8. Experimental vertical and horizontal semivariograms derived from the 1D HFEM and HTEM inversion results of the study area. Variography was performed in different directions (azimuths of 0°, 45°, 90° and 135°) with a tolerance of 22.5°. The manually fitted exponential models are also indicated.

Fig. 9. 3D view of kriging uncertainty on log-transformed resistivity. Displayed is the kriging standard deviation σ_{KRI} from the interpolation process of HFEM data. Low uncertainty traces (dark-blue) indicate the flight lines while the greatest uncertainty is across lines (rather than along lines).

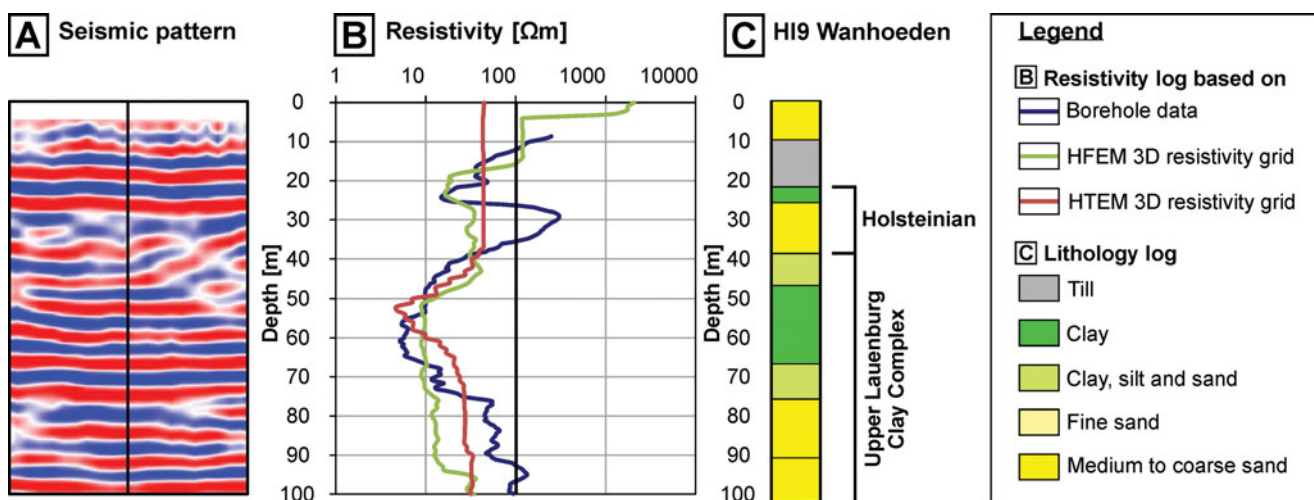
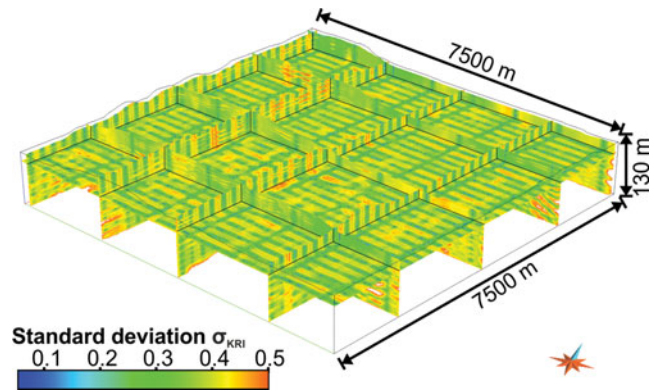


Fig. 10. Seismic section (A), resistivity log (B) and lithology log (C) of borehole HI9 Wanhoeden (after Besenecker, 1976). The blue curve shows the measured resistivity log of the borehole, the green curve displays the resistivity log extracted from the 3D HFEM resistivity grid and the red curve displays the projected resistivity log extracted from the 3D HTEM resistivity grid.

ogy resulted in the proportion of occurrences of each grain-size class per resistivity group (Fig. 11). As high resistivity values in the study area often represent dry sediments, we focused on resistivity values up to 250 Ωm .

Integration of the 3D resistivity grids with the 3D geological subsurface model

To test the match between the 3D resistivity grid models (based on 1D inversion results of AEM data) and the 3D geological subsurface model (based on borehole and seismic data), we integrated both into GOCAD (Fig. 3C). To verify the validity and accuracy of data and their integration we followed a mutual comparison between seismic reflector pattern and the corresponding resistivities obtained from the 3D AEM resistivity grids in GOCAD (Figs 4C and D Fig. 5C and D) and related grain-size

classes defined from borehole logs to resistivity values derived from the 3D AEM resistivity grid models (Fig. 11).

Adjustment of the 3D geological subsurface model

The GOCAD modelling software has various possibilities to visualise properties such as resistivity values of the 3D grid models to facilitate use and interpretation of data. This includes changes in the colour scale, the selection of given resistivity ranges and voxel volumes. The selection of specific resistivity ranges in the 3D resistivity grid model, in particular, provides a first rough estimate of the three-dimensional geological architecture (Fig. 3D).

In this study, we propose a method for 3D geological modelling of AEM data in which the limitations are jointly considered. The relationship between lithology and resistivity and its corresponding resistivity values was used to adjust the

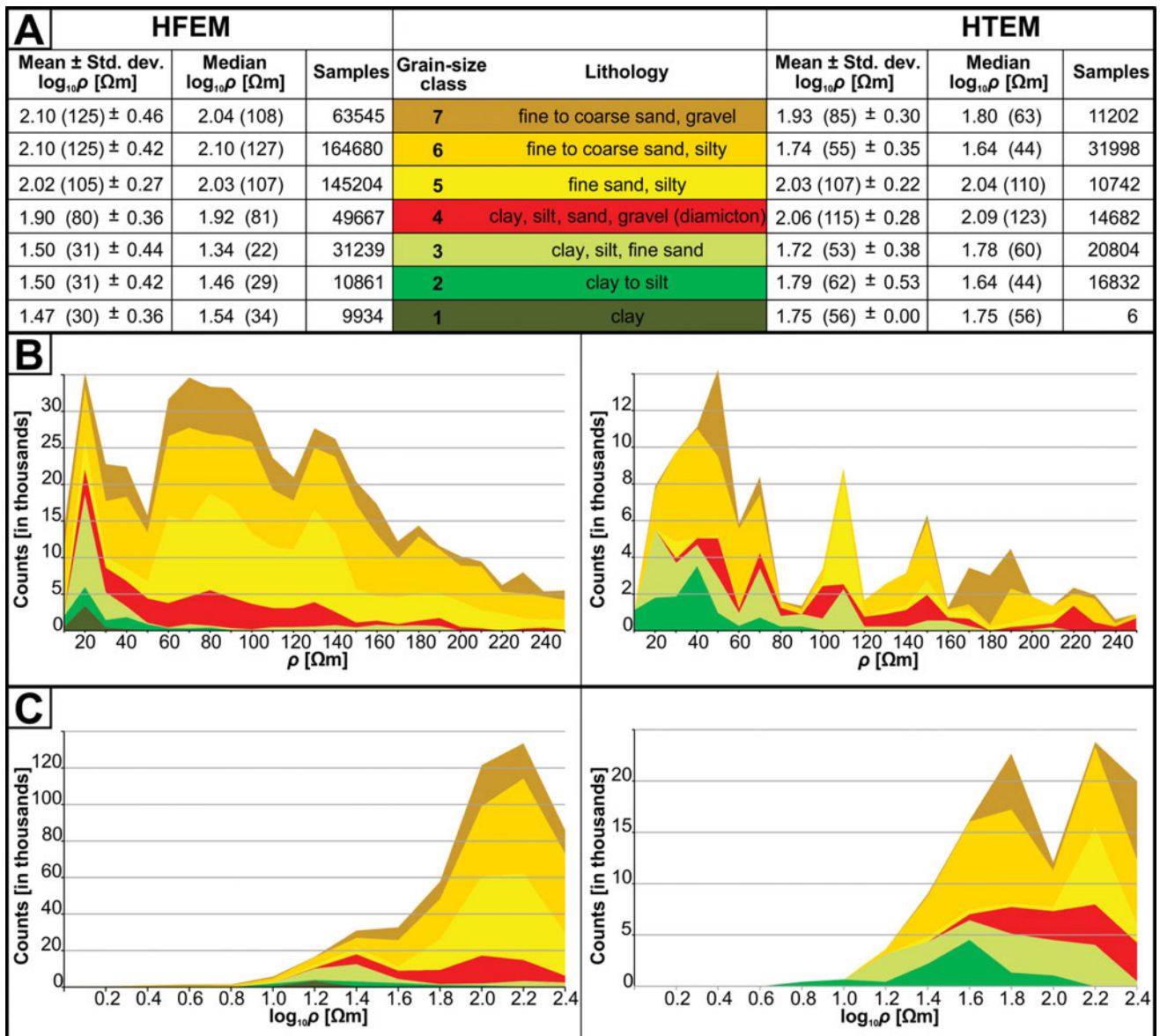


Fig. 11. Grain-size classes and related resistivity histograms extracted from the interpolated 3D HFEM and HTEM resistivity grid. A. Grain-size classes and related resistivity extracted from the interpolated 3D HFEM and HTEM resistivity grid. Shown are mean values, standard deviation, median values and number of counts for common resistivity (logarithmic values). B. Histogram showing resistivity classes of HFEM and HTEM data for each grain-size class as stacked bars (linear scale). C. Histogram showing resistivity classes of HFEM and HTEM data for each grain-size class as stacked bars (logarithmic scale). The absence of resistivity values lower than $1 \log_{10} \Omega\text{m}$ indicates that the influence of anthropogenic noise and saltwater can be excluded.

bounding surfaces of the geological framework model. After adjusting the geologic framework the updated 3D geological subsurface models were combined with the 3D HFEM voxel grid. Voxel grids can hold an unlimited number of attributes and different parameters can be added to the grid structure as attributes such as lithology, facies or model uncertainty. The high resolution of the regular voxel model allows the subsurface structure to be maintained. The result is a more reliable reconstruction of the shallow subsurface architecture (Figs 4–7). Nevertheless, internal lithology variations as identified on seis-

mic sections and the heterogeneity of sediments represented by overlapping resistivity ranges often leads to ambiguous lithological interpretation.

— **Verification of the 3D geological subsurface models by means of HFEM forward modelling**

We compared the apparent resistivity values at each frequency of the HFEM survey (Fig. 12A) with the apparent resistivity values derived from the initial 3D geological subsurface model

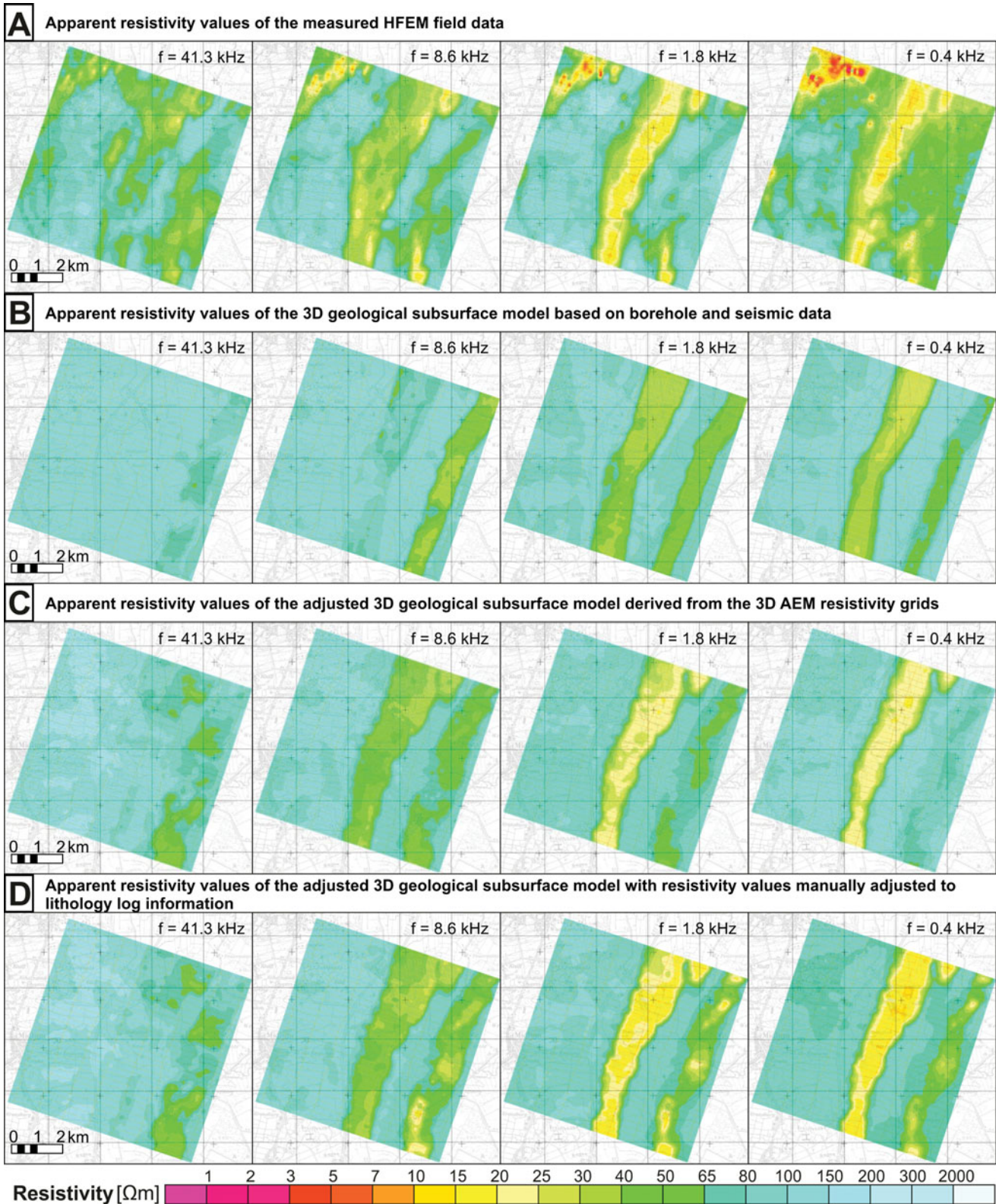


Fig. 12. Apparent resistivity images at different frequencies, corresponding to centroid depths, which increase from left to right. A. Apparent resistivity images of measured HFEM data. B. Apparent resistivity images extracted from the 3D geological subsurface model based on borehole and seismic data. C. Apparent resistivity images extracted from the adjusted 3D geological subsurface model derived from AEM data. D. Apparent resistivity images extracted from the adjusted 3D geological subsurface model derived from AEM data with manually adjusted resistivity values based on lithology log information.

based on borehole and seismic data (Fig. 12B) and the adjusted 3D geological subsurface model derived from the 3D AEM resistivity grids (Fig. 12C). This allowed identification of differences and uncertainties in each data set.

At each HFEM data point the thickness and median resistivity value of each geological unit derived from the different 3D geological subsurface models (Tables 1 and 2) were used to create a 1D resistivity model. For all 1D models, synthetic HFEM data were derived and transformed to apparent resistivity values at each HFEM frequency (Siemon, 2001). To verify the HFEM data, apparent resistivities were used to compare the measured and modelled HFEM data for two reasons: (1) the apparent resistivities are almost always independent of altitude variations of the HFEM system (Siemon et al., 2009a) and (2) they represent an approximation to the true resistivity distribution in the subsurface. The corresponding depth levels, however, vary as the centroid depth values depend on the penetration depth of the electromagnetic fields.

Results

The depositional architecture of the Cuxhaven tunnel valley and its Neogene host sediments defined by seismic and borehole data analysis

Neogene marine and marginal marine deposits The Neogene succession is 360 m thick and unconformably overlies open marine to paralic Oligocene deposits (Kuster, 2005). On the basis of previous investigations of the Neogene sedimentary successions (Gramann & Daniels, 1988; Odin & Kreuzer, 1988; Gramann, 1988, 1989; Overeem et al., 2001; Kuster, 2005; Köthe et al., 2008; Rumpel et al., 2009) four seismic units were mapped within the Neogene deposits, each bounded at the base by an unconformity. These seismic units can be correlated to seismic units in the North Sea Basin (Michelsen et al., 1998; Møller et al., 2009; Anell et al., 2012). The main characteristics of seismic units, including seismic facies, sedimentary facies and mean resistivity values are summarised in Table 1. The overall thickening observed in the westward dip direction of the seismic units is interpreted as an effect of the salt rim syncline subsidence creating accommodation space (cf. Maystrenko et al., 2005a,b; Grassmann et al., 2005; Brandes et al., 2012). The deposits consist of fine-grained shelf to marginal marine sediments.

At the end of the Miocene an incised valley formed that was subsequently filled with Pliocene delta deposits, probably indicating a palaeo-course of the River Weser or Elbe (Figs 4, 5 and 6). This is confirmed by the sub-parallel pattern of the lower valley fill onlapping reflector terminations onto the truncation surface observed in seismic lines S1 and S2. This is interpreted as transgressive backstepping (seismic lines S1 and S2; Table 1; Figs 4A and B, and 5A and B; Dalrymple et al., 1992).

The upper part of the incised-valley fill is characterised in the seismic by mound- and small-scale U-shaped elements, which are interpreted as prograding delta lobes (seismic lines S1 and S2; Figs 4A and B, and 5A and B).

Pleistocene and Holocene deposits Pleistocene deposits unconformably overly the marginal-marine Neogene sediments and are separated at the base by an erosional surface characterised by two steep-walled tunnel valleys passing laterally into sub-horizontal surfaces (Fig. 4A and B). The large tunnel valley is up to 350 m deep and 2 km wide (seismic line S1 and S2, Figs 4A and B, and 5A and B) and has previously been described by Kuster & Meyer (1979), Siemon et al. (2002, 2004), Gabriel et al. (2003), Siemon (2005), Wiederhold et al. (2005a), Gabriel (2006), Rumpel et al. (2009) and BurVal Working Group (2009). The smaller tunnel valley in the east is up to 200 m deep and 1 km wide (seismic line S1, Fig. 4A and B). In total, eight seismic subunits were mapped within these tunnel valleys and the marginal areas (U5.1–U5.8; cf. Table 2; Figs 4B and 5B). The main characteristics of seismic subunits, including seismic facies, sedimentary facies and mean resistivity values, are summarised in Table 2.

The dimension, geometry, internal reflector pattern and sedimentary fill of the troughs correspond well to Pleistocene tunnel-valley systems described from northern Germany (Ehlers & Linke, 1989; Stackebrandt, 2009; Lang et al., 2012; Janszen et al., 2013), Denmark (Jørgensen & Sandersen, 2009), the Netherlands (Kluiving et al., 2003) and the North Sea Basin (Wingfield, 1990; Huuse & Lykke-Andersen, 2000; Praeg, 2003; Lutz et al., 2009; Kehew et al., 2012; Moreau et al., 2012). The basal fill consists of Elsterian meltwater deposits overlain by glaciolacustrine deposits of the Lauenburg Clay Complex. These deposits are unconformably overlain by marine Holsteinian interglacial deposits. Saalian meltwater deposits and till cover the entire study area and unconformably overly the Neogene, Elsterian and Holsteinian deposits (Table 2; Figs 4A and B, and 5A and B).

Integration of the resistivity grid model and the geological subsurface model

Comparison of borehole resistivity logs with model resistivity data The borehole H19 Wanhoeden penetrates the western marginal tunnel-valley fill (cf. Figs 1C and 4B). The lowermost fill consists of Elsterian glaciolacustrine fine- to medium-grained sand and silt alternations of the Lower Lauenburg Clay Complex (U5.2–5.4). This succession is overlain by the Upper Lauenburg Clay Complex, which consists of clay, silt and fine-grained sand alternations (U5.5–5.6) and marine Holsteinian interglacial deposits (U5.7; Figs 4B and 10). The resistivity log of borehole H19 displays strong resistivity variations, which can be correlated with the alternation of clay- and sand-rich beds (Fig. 10). The 3D resistivity grid model based on 1D HFEM inversion results

displays a similar resistivity log as the one in the borehole and thus a good lithological match. The upper bounding surface of the Upper Lauenburg Clay Complex and the marine interglacial Holsteinian clay can also be identified on the 3D resistivity grid model (Fig. 10). The interpolated 3D resistivity grid model based on 1D HTEM inversion results, however, reveals only one conductor. While the Upper Lauenburg Clay Complex is nearly fully imaged, the interglacial marine Holsteinian clay is not well defined, which may be caused by the limited resolution of the transient electromagnetic (TEM) method. The highly conductive sediments of the Upper Lauenburg Clay Complex lead to a reduced penetration of the electromagnetic fields and hence resistivities of the sediments below the Upper Lauenburg Clay Complex are not detectable with the transmitter moments used in this survey.

An important difference between resistivity values of the measured resistivity log of borehole H19 and the extracted values from the 3D resistivity grid models based on 1D AEM inversion results is the amplitude of high resistivity values, which is considerably lower in the 3D resistivity grid models (Fig. 10). This difference can be explained by the applied AEM methods, which are more sensitive to conductive sediments (Steuer et al., 2009). In addition, the AEM system predominantly generates horizontal currents, whereas electromagnetic borehole systems use vertical currents for measuring the log resistivity. Sediment anisotropy as well as scaling effects has also to be taken into account.

Relationship between borehole lithology logs and AEM model resistivities Our analysis shows that resistivity generally increases with grain size and permeability, as also shown by Burschil et al. (2012b) and Klimke et al. (2013) for HTEM data. However, there are substantial differences between the borehole lithology and resistivity values derived from the two interpolated 3D AEM resistivity grids (Fig. 11). The 3D HFEM resistivity grid indicates that clay (grain-size class 1) has an average resistivity of 30 Ωm in the study area. This value corresponds to previous results of AEM data commonly reported in the literature for clay (Burschil et al., 2012b; Klimke et al., 2013). In comparison to borehole resistivity (commonly between 5 and 20 Ωm) the 3D HFEM resistivity value is slightly too high and may be caused (1) by a certain silt and sand content or (2) by the limited resolution of the HFEM method providing an over- or underestimated thickness or merging of lithological units. The average resistivity value for deposits mainly consisting of clay to silt is 31 Ωm (grain-size class 2), for clay- and silt-rich fine sand is 31 Ωm (grain-size class 3), for diamicton is 80 Ωm (grain-size class 4), for fine sand is 105 Ωm (grain-size class 5), for silt-rich fine to coarse sand is 125 Ωm (grain-size class 6) and for fine to coarse sand with gravel is 125 Ωm (grain-size class 7).

The relationship between borehole lithology and resistivity data extracted from the grid based on 1D HTEM inversion results does not allow the lithology to be clearly defined in 3D

(Fig. 11). The average resistivity value for clay from our data set (grain-size class 1) is 56 Ωm and may be skewed due to the small sample number. The average resistivity value for deposits mainly consisting of clay to silt is 62 Ωm (grain-size class 2), for clay- and silt-rich fine sand is 53 Ωm (grain-size class 3), for diamicton is 115 Ωm (grain-size class 4), for fine sand is 107 Ωm (grain-size class 5), for silt-rich fine to coarse sand is 55 Ωm (grain-size class 6) and for fine to coarse sand with gravel is 85 Ωm (grain-size class 7).

The histograms for both resistivity data sets (see Fig. 11) demonstrate that the measured values for sand are higher than for deposits with certain clay content. However, overlapping resistivity values for sand-dominated sediments and deposits with clay content are generally found to have a lower resistivity range, especially for the HTEM resistivity data set. The coarser-grained sediments (grain-size class 4 to 7) have a wide variety of resistivity values and seem too low, especially for the HTEM data set. Fig. 11 displays these large resistivity ranges. The variance in values is interpreted to result from the mixed lithological components, the limited resolution of the AEM system and the less distinctive imaging of low-conductive sediments.

The larger overlaps of HTEM resistivity values can be explained as an effect of restricted HTEM data coverage and the projection of interpolated resistivity values onto the borehole locations. Similar HTEM resistivity values were found at the island of Föhr (Burschil et al., 2012a,b) and for the region of Quakenbrück, southwestern Lower Saxony (Klimke et al., 2013). Nonetheless, discrimination of different lithologies with a wide range of resistivity values is possible by integrating with other data sets, for example borehole or seismic reflection data.

Correlation of the HFEM resistivity model with the geological model

Neogene marine and marginal marine deposits At depths between 10 and 120 m the spatial resistivity pattern is characterised by an elongated structure with gradual large-scale variations (100–300 m) of medium to high resistivity values that indicate the heterogeneous infill of the Late Miocene incised valley (seismic unit U4; Figs 4C and 5C). A positive correlation with the hummocky seismic reflector pattern and borehole lithology indicates that the resistivity pattern images grain-size variations of vertically and laterally stacked delta lobes (cf. Figs 4C and 5C).

Pleistocene deposits The difference in lithology between the fine-grained glacial Pleistocene deposits of the upper tunnel-valley fill and the coarser-grained Neogene marginal-marine sediments is expressed as a distinct resistivity contrast, which can be clearly traced in depth (Figs 4C, 5C and 6B).

The margin of the Cuxhaven tunnel valley is indicated by a gradual shift from low to medium resistivity values of Pleistocene deposits (seismic subunits U5.5, U5.6 and U5.7; Figs 4C,

5C, 6B and 7B) to higher resistivity values of the Pliocene host sediments (seismic unit U4; Figs 4C, 5C, 6B and 7B). The resistivity pattern of the HFEM model enables a good 3D imaging of the internal tunnel-valley fill. Large- and small-scale, elongated, wedge-shaped or lens-shaped variations in the resistivity pattern can be correlated with major seismic units and smaller-scale architectural elements, such as individual channels (cf. Fig. 4C: U5.7 between 3800 and 4000 m) and lobes (cf. Fig. 4C: U5.6 and U5.7 between 3600 and 3700 m).

The overall tabular geometry of the glaciolacustrine deposits of the Lauenburg Clay Complex (seismic subunit U5.6) and the marine Holsteinian interglacial deposits (seismic subunit U5.7) are both characterised by low resistivity values in the tunnel-valley centre (Figs 4C, 5C, 6B and 7B) and gradually into higher resistivity values towards the tunnel-valley margin. The higher resistivity values towards the tunnel-valley margin have been interpreted to be the result of bleeding of higher resistivity values from the neighbouring Pliocene sediments. Alternatively, they could be interpreted as an indicator for coarse-grained material (e.g. delta foresets at the margin of the tunnel valley in Fig. 5C: U5.2 and U5.4 between 700 and 800 m; in Fig. 4C: U5.5 at 4300 m and U5.6 at 4500 m). The comparison with lithology data from boreholes proves that the Lauenburg Clay Complex (seismic subunit U5.6) and the marine Holsteinian deposits (seismic subunit U5.7) are approximately imaged at the correct depths. The HFEM resistivity pattern, however, does not image a distinct boundary between the glaciolacustrine Lauenburg Clay Complex and the marine Holsteinian interglacial deposits due to their similar grain sizes.

Within the tunnel-valley centre thick conductive fine-grained beds of the Lauenburg Clay Complex limit the penetration depth of the HFEM system, leading to a decrease in resolution and a less distinct resistivity pattern of underlying fine- to medium-grained sand (cf. Fig. 5C, seismic subunit U5.5 in seismic line S2). Similar results have also been observed by Steuer et al. (2009).

In the eastern part of the study area lower resistivity values in HFEM data are identified, which differ from the Neogene host sediments. Its geometry and resistivity values suggest a smaller-scale tunnel valley and probably indicate a fill of fine-grained glaciolacustrine (Lauenburg Clay Complex) and/or interglacial marine (Holsteinian) deposits (Fig. 4C). The low resistivity contrast between this tunnel-valley fill and the Neogene host sediments probably indicates relatively similar grain sizes, but this remains speculative because no borehole log control is available.

In the uppermost part of the Pleistocene succession between 0 and 10 m depth (seismic subunit U5.8; Figs 4C and 5C) a distinct shift from low to very high resistivity values indicates a strong increase in electrical resistivity. This resistivity shift is interpreted to represent the transition between water saturated and unsaturated sediments – it represents the groundwater table contact. This strong resistivity contrast allows the detection

of the groundwater table within a range of approximately 2 m and clearly outlines the Hohe Lieth ridge as the most important groundwater recharge area, which has also been documented by Blindow & Balke (2005).

Correlation of the HTEM resistivity model with the geological model

Neogene marginal-marine deposits At depths between 180 and 150 m (seismic unit U3) the resistivity pattern is characterised by a sharp contrast from low to medium resistivity values (Figs 4D, 5D, 6B and 7B). This upward increase in resistivity is interpreted as an abrupt facies change from finer-grained shelf deposits to coarser-grained shoreface deposits, which is also recorded in borehole data (Kuster, 2005) and might be related to the rapid onset of progradation during the highstand systems tract.

Correlation of the resistivity pattern with borehole data indicates that the low resistivity values link to marine Early Tortonian clays (seismic unit U3). At depths between 120 and 80 m, large-scale, lateral variations of low to medium resistivity values, parallel to seismic reflections, can be identified. Altogether, resistivity contrast and seismic pattern, characterised by strong reflectivity contrasts, are interpreted to result from grain-size variations, which probably indicate the Tortonian to Messinian storm-dominated shoreface deposits (seismic unit U3; Table 1; Figs 4D and 5D; Walker & Plint, 1992; Catuneanu, 2002; Kuster, 2005; Catuneanu et al., 2011). Gradual vertical transitions from low to high resistivity values within the upper Neogene unit (seismic unit U4; Figs 4D and 5D) correspond to borehole lithology data with an overall coarsening-upward trend are interpreted as prograding delta lobes (e.g. Dalrymple et al., 1992; Plink-Björklund, 2008). This interpretation is further supported by the seismic pattern of lobate units (Figs 4A and B and 5A and B).

Pleistocene deposits The lithology contrast between the fine-grained glacial Pleistocene deposits at the base and the underlying coarser-grained Neogene marginal-marine sediments is expressed as a distinct change in resistivity, which can be clearly traced in the shallow subsurface between 20 and 30 m depth and corresponds to the lower boundary of seismic unit U5 (Figs 4D and 5D). The tunnel-valley margin can be identified in borehole data, but in the deeper subsurface is not clearly imaged by the HTEM resistivity data. At the tunnel-valley margin the resistivity resembles that of the adjacent Neogene host sediments and therefore its boundary may not be as easily distinguished (Figs 4D, 5D, 6C and 7C). The inability for the HTEM data to have contrasting resistivity values to define the tunnel-valley boundary is probably caused by the large lateral footprint of the HTEM system, the inversion approach (SCI) and the kriging method, which leads to a smooth transition between individual resistivity values.

The upper Cuxhaven tunnel-valley fill is characterised by different vertically stacked resistivity patterns. The highly conductive sediments of the Lauenburg Clay Complex lead to a reduced penetration of the EM field and the resistivity of the sediments below are not detectable with the transmitter moments used in this survey. This suggests that the medium resistivity values imaged at depths between 160 and 80 m do not necessarily show the true resistivities of Pleistocene sand within the tunnel valley recorded in borehole data (seismic subunits U5.1 to U5.4; Figs 4D and 5D). However, the distinct shift towards higher resistivity values in the unit below the highly conductive sediments of the Lauenburg Clay Complex probably indicates coarser-grained deposits of seismic subunit U5.5 (Figs 4D and 5D). At depths between 80 and 10 m low resistivity values can be correlated with fine-grained glaciolacustrine sediments of the Lauenburg Clay Complex and interglacial Holsteinian deposits (seismic subunit U5.6 and U5.7; Figs 4D and 5D). The comparison of the resistivity data with the borehole logs and seismic data (Fig. 5B) indicates that resistivity changes reflect lithological changes.

Verification of apparent resistivity values extracted from the 3D subsurface models

The comparison of the apparent resistivity values derived from the HFEM data (Fig. 12A), the initial geological subsurface model based on borehole and seismic data (Fig. 12B), and the adjusted geological subsurface model derived from the 3D AEM resistivity grids (Fig. 12C) generally show a relationship indicating that both geological models are able to explain the principal resistivity distribution at several HFEM frequencies. The apparent resistivity images of the initial 3D geological subsurface model show a relatively sharp resistivity contrast between the Pleistocene tunnel valley and the adjacent Neogene deposits (Fig. 12B), particularly at the lower frequencies (at greater depths) defining a simple tunnel-valley geometry with a low sinuosity. The apparent resistivity map derived from the initial 3D geological subsurface model (Fig. 12B), however, does not image the tunnel-valley fill at the highest frequency (at shallow depths). The difference between the apparent resistivity images can be explained by the limited coverage of borehole and seismic data, which leads to restricted information about the subsurface architecture. The apparent resistivity images of the adjusted 3D geological subsurface model derived from the 3D AEM resistivity grids (Fig. 12C) show a more complex tunnel-valley geometry characterised by a higher sinuosity and smaller-scale variations of the resistivity pattern. This more complex interpretation of the tunnel valley can be better aligned with the apparent resistivity images of HFEM data (Fig. 12A) and the lithology variations recorded by borehole data. Nevertheless, uncertainties remain and are caused by the decreasing resolution with depth, which may lead to less contrast in the resistivity images. This is especially apparent at the

lowest frequency, whereby the resistivity images are influenced by underlying sediments. This often leads to the bottom layer of the 1D inversion models being represented by incorrect resistivity values. To reduce this problem we manually adjusted the resistivity values of bottom units in the adjusted 3D geological subsurface model derived from the 3D AEM resistivity grids based on lithology information (i.e. in particular the resistivity value for the lower part of unit U3 representing clay and silt was reduced by a factor of about 2; cf. Table 1). The resistivities of the valley infill were adjusted if the calculated mean values were misleading for the sediment type (i.e. too high resistivities attributed to clay and silt units were reduced, e.g. seismic subunit U5.3, and too low resistivities attributed to sandy units were increased, e.g. seismic subunits U5.1 and U5.4; cf. Table 2). Some other values were rounded.

We re-calculated the apparent resistivity values after correction (Fig. 12D). These resistivity images better represent the subsurface architecture and are closer to the apparent resistivity maps represented in the HFEM data, i.e. the adjusted geological model better explains the HFEM data. Nevertheless, differences in the images of the apparent resistivity patterns remain. This is caused by a too low resolution of the 3D geological subsurface model, which does not represent detailed sediment variability, and incorrectly estimated resistivities attributed to the geological units. A good example of this effect is the area of the smaller tunnel valley in the eastern part of the study area (Fig. 12D), where the clay and silt deposits (lower part of U3) are obviously thinner or/and resistive, and the central part of the valley fill U5.5* was estimated as too broad and too conductive. On the other hand, the low apparent resistivities in the northwest of the study area, which occur particularly at low frequencies, are caused by anthropogenic sources (airport Cuxhaven/Nordholz).

Discussion

Our results show that AEM data provide excellent opportunities to map the subsurface geology as previously demonstrated by, for example, Newman et al. (1986), Jordan & Siemon (2002), Danielsen et al. (2003), Jørgensen et al. (2003b, 2013), Auken & Christiansen (2004), Auken et al. (2008), Viezzoli et al. (2008), Bosch et al. (2009), Christensen et al. (2009), Klimke et al. (2013) and Gunnink & Siemon (2014). A good relationship between resistivity values and lithology enables the 3D imaging of the subsurface architecture. This allows a hitherto unseen amount of geological detail using AEM data in areas of low borehole coverage. This approach provides an advanced 3D geological model of the study area with new geological insights. Although the presented approach is more time-consuming than an automated approach that relies on statistics-based methods (Bosch et al., 2009; Gunnink et al., 2012), the

end results compensate for the limitations of the AEM method.

Geological and geophysical models and their interpretations contain limitations and uncertainties resulting from limitations in the input information (Ross et al., 2005). Several studies focussed on the analysis of such limitations and uncertainties in order to minimise risk, e.g. exploration risks (Bárdossy & Fodor, 2001; Pryet et al., 2011; Wellmann & Regenauer-Lieb, 2012; Jørgensen et al., 2013). Uncertainties and limitations in the integrated interpretation of AEM and ground-based data are mainly caused by the restricted availability and limited vertical and lateral resolution of data (e.g. boreholes, seismic sections, airborne surveys), modelling errors caused by a misinterpretation of geophysical, lithological and hydrogeological properties, anthropogenic noise effects, missing software interoperability (Mann, 1993; Bárdossy & Fodor, 2001; Ross et al., 2005; Pryet et al., 2011) and irreducible, input-geology related, uncertainty. In general there are several limitations in the interpretation caused by the applied AEM systems and the chosen data analysis.

The penetration depth and resolution of both AEM systems used is controlled by lithology and their conductivity. The penetration depth is limited to approximately 100 m for HFEM and 250 m for HTEM, and both systems are subject to decreasing resolution capability with depth and require an increasing thickness/depth ratio for the detection of varying depositional units (Jørgensen et al., 2003b, 2005; Høyer et al., 2011). Because of the wide range of lithologies a significant uncertainty remains in the final interpretation of the resistivity pattern. Hence, thin-bedded sedimentary units are only resolved if their corresponding conductance, i.e. the ratio of thickness and resistivity, is sufficiently high. Otherwise they will be merged into a single unit with an average resistivity (Jørgensen et al., 2003b, 2005), which results in a limited resistivity resolution. The limitations in lateral and vertical resolution can lead to incorrect interpretations of thin-bedded sand/mud couplets, smaller-scale architectural elements and bounding surfaces, as has been also shown by, for example, Jørgensen et al. (2003a, 2005), Viezzoli et al. (2008), Christensen et al. (2009) and Klimke et al. (2013). This problem is distinctly seen in our study area in the Pleistocene tunnel valley and Late Miocene incised valley. The Saalian till at 20 m depth with a thickness between 5 and 10 m and a wide resistivity range (cf. Fig. 11) could not be differentiated from the surrounding lithology and is beyond the possible AEM resolution. The Pleistocene tunnel-valley margins and the Late Miocene incised-valley margin could not be detected because of a low resistivity contrast to the adjacent Neogene host sediments.

For our study only an existing 1D AEM inversion data set (from 2002) was available, in which noise effects were not significantly minimised, as commonly applied for new data sets (e.g. Tølbøll, 2007; Siemon et al., 2011). However, the noise effects of anthropogenic structures and soundings in the

airborne electromagnetic data can hinder a proper geological interpretation, e.g. the airport Cuxhaven/Nordholz located in the northwest of the study area. In the case of the study area anthropogenic noise effects cause unrealistic low resistive oscillations, which conically increase downwards.

We used a geostatistical approach to analyse and interpolate the 1D AEM inversion results to create a continuous 3D resistivity subsurface grid. We used ordinary kriging, and in contrast to Pryet et al. (2011) we discarded the layered approach used in the 1D inversion of AEM data, leading to a smoothing effect between previously defined layer boundaries. The advantage of this method is that the kriging algorithm indicates the most likely resistivity value at each grid cell. The result is an effectively smoothed resistivity grid, leading to a significant improved geological interpretation of continuous lithofacies. However, a loss of heterogeneity that is probably observed in the subsurface by AEM has to be taken into account. If the aim is to generate fluid-flow models it is important to preserve the porosity and permeability of varying lithologies as these strongly determine fluid-flow behaviour through porous media (e.g. Koltermann & Gorelick, 1996; Janszen, 2012). It is therefore preferred to base fluid-flow simulations on grids that are interpolated using algorithms that are able to preserve the heterogeneity, such as modified kriging methods like the sequential indicator simulation used by Venteris (2007), Bosch et al. (2009) and Janszen (2012).

A common limitation of the presented workflow is the high degree of subjectivity that causes uncertainties that are hard to evaluate. To test the reliability of the 3D geological subsurface model and evaluate uncertainty, we followed a new approach to derive synthetic HFEM data from the geological model results based on a relationship of calculated or assumed geological units and resistivities. The comparison between corresponding apparent resistivity images of the subsurface based on AEM field measurements and 3D geological models leads to the identification of uncertainties and limitations of 1D AEM inversion and vice versa. The results of such analyses will offer the advantage of using a priori information to improve the inversion of AEM data, comparable to investigations made by, for example, Zhdanov (2010) and Gunnink et al. (2012).

Conclusions

Resistivity data derived from AEM surveys can provide a fast and efficient overview mapping of the shallow subsurface geology. A methodology for the interpretation, analysis and imaging of resistivity data gained by AEM surveys, based on 3D modelling approaches, was developed. We used 1D HFEM and HTEM inversion results and applied a 3D resistivity gridding procedure based on geostatistical analyses and interpolation techniques to create continuous resistivity models of the subsurface. Subsequently, we integrated results of seismic facies and borehole lithology

analysis to construct a combined 3D geological subsurface model and to reduce uncertainties. This approach allows for an improved interpretation of AEM data and imaging of the 3D subsurface architecture, if the relationship between lithology and resistivity was known and the site was only slightly influenced by noise effects (e.g. infrastructural networks, settlements).

The 3D resistivity models clearly allow discrimination between different lithologies and enable the detection of Cenozoic sequence boundaries and larger-scale architectural elements such as incised valleys and subglacial tunnel valleys. Variations in the resistivity pattern allowed the detection of individual delta lobes and smaller-scale channels as well as lateral and vertical grain-size variations. In the Neogene succession a low resistive pattern can be correlated with Tortonian and Messinian marine clays. The lowest values probably correspond with the zone of maximum flooding. From seismic interpretation we conclude that at the end of the Miocene an incised valley formed as a response to a major sea-level fall that subsequently became filled with Pliocene-delta deposits, probably indicating the palaeo-course of the Rivers Weser or Elbe. The resistivity models clearly image the outline of the Pleistocene tunnel valleys. The unconsolidated fill of the Late Miocene to Pliocene incised valley probably formed a preferred pathway for the Pleistocene meltwater flows, favouring the incision of a subglacial tunnel valley. Based on the 3D HFEM resistivity grid the fills of the tunnel valleys could be imaged in much more detail in comparison to previously published descriptions based on the 2D seismic sections and 2D AEM profiles and maps. The applied approaches and results show a reliable methodology, especially for future investigations of similar geological settings.

Acknowledgements

The AIDA project is part of the joint research program of GEOTECHNOLOGIEN. Financial support is gratefully acknowledged from the German Federal Ministry of Education and Research (BMBF) grant 03G0735. We thank two anonymous reviewers for very careful and constructive reviews, which helped to improve the manuscript. Many thanks are due to Hajo Götze and Peter Menzel for discussion, and Guillaume Martelet for helpful comments on an earlier version of the manuscript and Ariana Osman for discussion and improving the English. We are grateful to the State Authority for Mining, Energy and Geology (LBEG) for providing borehole data, to Fugro for providing the GeODin software and Paradigm for GOCAD software support.

References

- Anell, I., Thybo, H. & Rasmussen, E.**, 2012. A synthesis of Cenozoic sedimentation in the North Sea. *Basin Research* 24: 154–179.
- Archie, G.E.**, 1942. The electrical resistivity log as an aid in determining some reservoir characteristics. *Trans AIME* 146: 54–62.
- Auken, E. & Christiansen, A.V.**, 2004. Layered and laterally constrained 2D inversion of resistivity data. *Geophysics* 69(3): 752–761.
- Auken, E., Christiansen, A.V., Jacobsen, L.H. & Sorensen, K.I.**, 2008. A resolution study of buried valleys using laterally constrained inversion of TEM data. *Journal of Applied Geophysics* 65(1): 10–20.
- Baldschuhn, R., Frisch, U. & Kockel, F.** (eds), 1996. *Geotektonischer Atlas von NW-Deutschland 1 : 300000*. Bundesanstalt für Geowissenschaften und Rohstoffe (Hannover).
- Baldschuhn, R., Binot, F., Fleig, S. & Kockel, F.**, 2001. *Geotektonischer Atlas von Nordwestdeutschland und dem deutschen Nordsee-Sektor*. Geologisches Jahrbuch A153: 3–95.
- Bárdossy, G. & Fodor, J.**, 2001. Traditional and new ways to handle uncertainty in geology. *Natural Resources Research* 10(3): 179–187.
- Besenecker, H.**, 1976. Bohrdatenbank Niedersachsen, Bohr-ID: 3028HY0304, Landesamt für Bergbau, Energie und Geologie (LBEG) (Hannover).
- Betz, D., Führer, F., Greiner, G. & Plein, E.**, 1987. Evolution of the Lower Saxony Basin. *Tectonophysics* 137: 127–170.
- Binot, F. & Wonik, T.**, 2005. Lithologie und Salz-/Süßwassergrenze in der Forschungsbohrung Cuxhaven Lüdingworth 1/1A. *Zeitschrift für Angewandte Geologie* 1: 14–23.
- Blindow, N. & Balke, J.**, 2005. GPR-Messungen zur Bestimmung der Grundwasser-oberfläche im Bereich des Geestrückens südlich von Cuxhaven. *Zeitschrift für Angewandte Geologie* 1: 39–44.
- Bosch, J.H.A., Bakker, M.A.J., Gunnink, J.L. & Paap, B.F.**, 2009. Airborne electromagnetic measurements as basis for a 3D geological model of an Elsterian incision. *Zeitschrift der deutschen Gesellschaft für Geowissenschaften* 160(3): 249–258.
- Brandes, C., Pollok, L., Schmidt, C., Riegel, W., Wilde, V. & Winsemann, J.**, 2012. Basin modelling of a lignite-bearing salt rim syncline: insights into rim syncline evolution and salt diapirism in NW Germany. *Basin Research* 24: 699–716.
- Burschil, T., Wiederhold, H. & Auken, E.**, 2012a. Seismic results as a-priori knowledge for airborne TEM data inversion – A case study. *Journal of Applied Geophysics* 80: 121–128.
- Burschil, T., Scheer, W., Kirsch, R. & Wiederhold, H.**, 2012b. Compiling geophysical and geological information into a 3-D model of the glacially-affected island of Föhr. *Hydrology and Earth System Sciences* 16: 3485–3498.
- BurVal Working Group**, 2009. Buried Quaternary valleys - a geophysical approach. *Zeitschrift der deutschen Gesellschaft für Geowissenschaften* 160(3): 237–247.
- Cameron, T.D.J., Buat, J. & Mesdag, C.S.**, 1993. High resolution seismic profile through a Late Cenozoic delta complex in the southern North Sea. *Marine and Petroleum Geology* 10: 591–599.
- Caspers, G., Jordan, H., Merkt, J., Meyer, K.-D., Müller, H. & Streif, H.**, 1995. III. Niedersachsen. In: Benda, L. (ed.): *Das Quartär Deutschlands*. Gebrüder Bornträger (Berlin): 23–58.
- Catuneanu, O.**, 2002. Sequence stratigraphy of clastic systems: concepts, merits, and pitfalls. *Journal of African Earth Sciences* 35: 1–43.
- Catuneanu, O., Galloway, W.E., Kendall, C.G.St.C., Miall, A.D., Posamentier, H.W., Strasser, A. & Tucker, M.E.**, 2011. *Sequence Stratigraphy: Methodology and Nomenclature*. *Newsletters on Stratigraphy* 44(3): 173–245.
- Christensen, N.B., Reid, J.E. & Halkjær, M.**, 2009. Fast, laterally smooth inversion of airborne time-domain electromagnetic data. *Near Surface Geophysics* 7: 599–612.

- Dalrymple, R.W., Zaitlin, B.A. & Boyd, R.**, 1992. Estuarine facies models: conceptual basis and stratigraphic implications. *Journal of Sedimentary Petrology* 62: 1130–1146.
- Danielsen, J.E., Auken, E., Jørgensen, F., Søndergård, V. & Sørensen, K.I.**, 2003. The application of the transient electromagnetic method in hydrogeological surveys. *Journal of Applied Geophysics* 53: 181–198.
- de Louw, P.G.B., Eeman, S., Siemon, B., Voortman, B.R., Gunnink, J., van Baaren, E.S. & Oude Essink, G.H.P.**, 2011. Shallow rainwater lenses in deltaic areas with saline seepage. *Hydrology Earth System Sciences* 15: 3659–3678.
- Ehlers, J.**, 2011. Geologische Karte von Hamburg 1: 25 000: Erläuterungen zu Blatt Nr. 2326 Fuhsbüttel. Behörde für Stadtentwicklung und Umwelt, Geologisches Landesamt Hamburg (Hamburg).
- Ehlers, J. & Linke, G.**, 1989. The origin of deep buried channels of Elsterian age in northwest Germany. *Journal of Quaternary Science* 4: 255–265.
- Ehlers, J., Meyer, K.-D. & Stephan, H.-J.**, 1984. Pre-weichselian glaciations of north-west Europe. *Quaternary Science Reviews* 3: 1–40.
- Ehlers, J., Grube, A., Stephan, H.-J. & Wansa, S.**, 2011. Pleistocene Glaciations of North Germany – New Results. In: Ehlers, J., Gibbard, P.L. & Hughes, P.D. (eds): *Quaternary Glaciations – Extent and Chronology – A Closer Look. Developments in Quaternary Science* 15. Elsevier (Amsterdam): 149–162.
- Eidvin, T. & Rundberg, Y.**, 2007. Post-Eocene strata of the southern Viking Graben, northern North Sea; integrated biostratigraphic, strontium isotopic and lithostratigraphic study. *Norwegian Journal of Geology* 87: 391–450.
- Fraser, D.C.**, 1978. Resistivity mapping with an airborne multicoil electromagnetic system. *Geophysics* 43: 144–172.
- Fugro Consult GmbH**, 2012. GeODin 7, <http://www.geodin.com>. Berlin, Germany.
- Gabriel, G.**, 2006. Gravity investigation of buried Pleistocene subglacial valleys. *Near Surface Geophysics* 4: 321–332.
- Gabriel, G., Kirsch, R., Siemon, B. & Wiederhold, H.**, 2003. Geophysical investigations of buried Pleistocene subglacial valleys in Northern Germany. *Journal of Applied Geophysics* 53: 159–180.
- Gast, R. & Gundlach, T.**, 2006. Permian strike slip and extensional tectonics in Lower Saxony, Germany. *Zeitschrift der Deutschen Gesellschaft für Geowissenschaften* 157(1): 41–55.
- Gibbard, P.L.**, 1988. The history of the great northwest European rivers during the past three million years. *Philosophical Transactions of the Royal Society of London B* 318: 559–602.
- Gramann, F.**, 1988. Major palaeontological events and biostratigraphical correlations. *Geologisches Jahrbuch A100*: 410–423.
- Gramann, F.**, 1989. Forschungsbohrung Wursterheide. Benthonische Foraminiferen und verwandte Mikrofossilien. Biostratigraphie, Faziesanalyse. *Geologisches Jahrbuch A111*: 287–319.
- Gramann, F. & Daniels, C.H. von**, 1988. Benthic foraminifera: the description of the interregional zonation (B zones). *Geologisches Jahrbuch A100*: 145–151.
- Gramann, F. & Kockel, F.**, 1988. Palaeogeographical, lithological, palaeoecological and palaeoclimatic development of the Northwest European Tertiary Basin. *Geologisches Jahrbuch A100*: 428–441.
- Grassmann, S., Cramer, B., Delisle, G., Messner, J. & Winsemann, J.**, 2005. Geological history and petroleum system of the Mittelplate oil field, Northern Germany. *International Journal of Earth Sciences* 94: 979–989.
- Gunnink, J.L. & Siemon, B.**, 2014. Applying airborne electromagnetics in 3D stochastic geohydrological modelling for determining groundwater protection. *Near Surface Geophysics*, 12 (early online), doi: 10.3997/1873-0604.2014044. EAGE Publications (Houten).
- Gunnink, J.L., Bosch, J.H.A., Siemon, B., Roth, B. & Auken, E.**, 2012. Combining ground-based and airborne EM through artificial neural networks for modelling hydrogeological units under saline groundwater conditions. *Hydrology and Earth System Sciences* 16: 3061–3074.
- Haq, B.U., Hardenbol, J. & Vail, P.R.**, 1987. Chronology of fluctuating sea levels since the Triassic (250 million years ago to present). *Science* 235: 1156–1167.
- Hese, F.**, 2012. 3D Modellierungen und Visualisierung von Untergrundstrukturen für die Nutzung des unterirdischen Raumes in Schleswig-Holstein. PhD thesis, Christian-Albrechts-Universität zu Kiel (Kiel).
- HGG**, 2011. Guide to processing and inversion of SkyTEM data in the Aarhus Workbench. Technical report, Hydro-Geophysical Group, Department of Earth Sciences, University of Aarhus (Aarhus).
- Höfle, H.C., Merkt, J. & Müller, H.**, 1985. Die Ausbreitung des Eem-Meeres in Nordwestdeutschland. *Eiszeitalter und Gegenwart* 35: 49–59.
- Høyer, A.-S., Lykke-Andersen, H., Jørgensen, F. & Auken, E.**, 2011. Combined interpretation of SkyTEM and high-resolution seismic data. *Journal of Physics and Chemistry of the Earth* 36(16): 1386–1397.
- Huuse, M.**, 2002. Late Cenozoic palaeogeography of the eastern North Sea Basin climatic vs. tectonic forcing of basin margin uplift and deltaic progradation. *Bulletin of the Geological Society of Denmark* 49: 145–170.
- Huuse, M. & Clausen, O.R.**, 2001. Morphology and origin of major Cenozoic sequence boundaries in the eastern North Sea Basin: top Eocene, near-top Oligocene and the mid-Miocene unconformity. *Basin Research* 13: 17–41.
- Huuse, M. & Lykke-Andersen, H.**, 2000. Overdeepened Quaternary valleys in the eastern Danish North Sea: morphology and origin. *Quaternary Science Reviews* 19: 1233–1253.
- Huuse, M., Lykke-Andersen, H. & Michelsen, O.**, 2001. Cenozoic evolution of the eastern North Sea Basin – new evidence from high-resolution and conventional seismic data. *Marine Geology* 177: 243–269.
- Huuse, M., Piotrowski, J.A. & Lykke-Andersen, H.**, 2003. Geophysical investigations of buried Quaternary valleys in the formerly glaciated NW European lowland: significance for groundwater exploration. *Journal of Applied Geophysics* 53: 153–157.
- Janszen, A.**, 2012. Tunnel valleys: genetic models, sedimentary infill and 3D architecture. PhD thesis, Delft University of Technology (Delft).
- Janszen, A., Spaak, M. & Moscariello, A.**, 2012. Effects of the substratum on the formation of glacial tunnel valleys: an example from the Middle Pleistocene of the southern North Sea Basin. *Boreas* 41: 629–643.
- Janszen, A., Moreau, J., Moscariello, A., Ehlers, J. & Kröger, J.**, 2013. Time-transgressive tunnel-valley infill revealed by a three-dimensional sedimentary model, Hamburg, north-west Germany. *Sedimentology* 60(3): 693–719.
- Jaritz, W.**, 1987. The origin and development of salt structures in Northwest Germany. In: Lerche, I. & O'Brian, J.J. (eds): *Dynamical Geology of Salt and Related Structures*. Academic Press (Orlando): 479–493.
- Jordan, H. & Siemon, B.**, 2002. Die Tektonik des nordwestlichen Harzrandes – Ergebnisse der Hubschrauber-Elektromagnetik. *Zeitschrift der Deutschen Geologischen Gesellschaft* 153(1): 31–50.
- Jørgensen, F. & Sandersen, P.B.E.**, 2006. Buried and open tunnel valleys in Denmark – erosion beneath multiple ice sheets. *Quaternary Science Reviews* 25: 1339–1363.

- Jørgensen, F. & Sandersen, P.B.E.**, 2009. Buried valley mapping in Denmark: evaluating mapping method constraints and the importance of data density. *Zeitschrift der deutschen Gesellschaft für Geowissenschaften* 160(3): 211–229.
- Jørgensen, F., Lykke-Andersen, H., Sandersen, P.B.E., Auken, E. & Nørmark, E.**, 2003a. Geophysical investigations of buried Quaternary valleys in Denmark: an integrated application of transient electromagnetic soundings, reflection seismic surveys and exploratory drillings. *Journal of Applied Geophysics* 53: 215–228.
- Jørgensen, F., Sandersen, P.B.P. & Auken, E.**, 2003b. Imaging buried valleys using the transient electromagnetic method. *Journal of Applied Geophysics* 53: 215–228.
- Jørgensen, F., Sandersen, P.B.P., Auken, E., Lykke-Andersen, H. & Sørensen, K.**, 2005. Contributions to the geological mapping of Mors, Denmark – A study based on large-scale TEM survey. *Bulletin of the Geological Society of Denmark* 52: 53–75.
- Jørgensen, F., Rønde Møller, R., Nebel, L., Jensen, N.-P., Christiansen, A.V. & Sandersen, P.B.E.**, 2013. A method for cognitive 3D geological voxel modelling of AEM data. *Bulletin of Engineering Geology and the Environment* 72(3–4): 421–432.
- Jürgens, U.**, 1996. Mittelmiozäne bis pliozäne Randmeer-Sequenzen aus dem deutschen Sektor der Nordsee. *Geologisches Jahrbuch A146*: 217–232.
- Kehew, A.E., Piotrowski, J.A. & Jørgensen, F.**, 2012. Tunnel valleys: Concepts and controversies – A review. *Earth-Science Reviews* 113: 33–58.
- Klimke, J., Wiederhold, H., Winsemann, J., Ertl, G. & Elbracht, J.**, 2013. Three-dimensional mapping of Quaternary sediments improved by airborne electromagnetics in the case of the Quakenbrück Basin, Northern Germany. *Zeitschrift der deutschen Gesellschaft für Geowissenschaften* 164(2): 369–384.
- Kluiving, S.J., Bosch, J.H.A., Ebbing, J.H.J., Mesdag, C.S. & Westerhoff, R.S.**, 2003. Onshore and offshore seismic and lithostratigraphic analysis of a deeply incised Quaternary buried valley-system in the Northern Netherlands. *Journal of Applied Geophysics* 53: 249–271.
- Knox, R.W.O.B., Bosch, J.H.A., Rasmussen, E.S., Heilmann-Clausen, C., Hiss, M., De Lugt, I.R., Kasiński, J., King, C., Köthe, A., Słodkowska, B., Standke, G. & Vandenberghe, N.**, 2010. Cenozoic. In: Doornenbal, J.C. & Stevenson, A.G. (eds): *Petroleum Geological Atlas of the Southern Permian Basin Area*. EAGE Publications b.v. (Houten): 211–223.
- Knudsen, K.L.**, 1988. Marine Interglacial Deposits in the Cuxhaven Area, NW Germany: A Comparison of Holsteinian, Eemian and Holocene Foraminiferal Faunas. *Eiszeitalter und Gegenwart* 38: 69–77.
- Knudsen, K.L.**, 1993a. Foraminiferal Faunas in Holsteinian Deposits of the Neuwerk Area, Germany. *Geologisches Jahrbuch A138*: 77–95.
- Knudsen, K.L.**, 1993b. Late Elsterian-Holsteinian Foraminiferal Stratigraphy in Boreholes in the Lower Elbe Area, NW Germany. *Geologisches Jahrbuch A138*: 97–119.
- Kockel, F.**, 2002. Rifting processes in NW-Germany and the German North Sea Sector. *Netherlands Journal of Geosciences/Geologie en Mijnbouw* 81: 149–158.
- Koltermann, C.E. & Gorelick, S.M.**, 1996. Heterogeneity in sedimentary deposits: a review of structure-imitating, process-imitating, and descriptive approaches. *Water Resources Research* 32: 2617–2658.
- Konradi, P.**, 2005. Cenozoic stratigraphy in the Danish North Sea Basin. *Geologie en Mijnbouw* 84: 109–111.
- Köthe, A.**, 2007. Cenozoic biostratigraphy from the German North Sea sector (G-11-1 borehole, dinoflagellate cysts, calcareous nannoplankton). *Zeitschrift der deutschen Gesellschaft für Geowissenschaften* 158(2): 287–327.
- Köthe, A., Gaedicke, C. & Rüdiger, L.**, 2008. Erratum: The age of the Mid-Miocene Unconformity (MMU) in the G-11-1 borehole, German North Sea sector. *Zeitschrift der deutschen Gesellschaft für Geowissenschaften* 159(4): 687–689.
- Krige, D.G.**, 1951. A statistical approach to some basic mine valuation problems on the Witwatersrand. *Journal of the Chemical, Metallurgical and Mining Society of South Africa* 52(6): 119–139.
- Kuhlmann, G., de Boer, P., Pedersen, R.B. & Wong, Th.E.**, 2004. Provenance of Pliocene sediments and paleoenvironmental changes in the southern North Sea region using Samarium-Neodymium (Sm/Nd) provenance ages and clay mineralogy. *Sedimentary Geology* 171: 205–226.
- Kuhlmann, G. & Wong, T.E.**, 2008. Pliocene paleoenvironment evolution as interpreted from 3D-seismic data in the southern North Sea, Dutch offshore sector. *Marine and Petroleum Geology* 25: 173–189.
- Kuster, H.**, 2005. Das jüngere Tertiär in Nord- und Nordostniedersachsen. *Geologisches Jahrbuch A158*: 0–194.
- Kuster, H. & Meyer, K.-D.**, 1979. Glaziäre Rinnen im mittleren und nordöstlichen Niedersachsen. *Eiszeitalter und Gegenwart* 29: 135–156.
- Kuster, H. & Meyer, K.-D.**, 1995. Quartärgeologische Übersichtskarte von Niedersachsen und Bremen, 1 : 500 000. Niedersächsisches Landesamt für Bodenforschung (Hannover).
- Lane, R., Green, A., Golding, C., Owers, M., Pik, P., Plunkett, C., Sattel, D. & Thorn, B.**, 2000. An example of 3D conductivity mapping using the TEMPEST airborne electromagnetic system. *Exploration Geophysics* 31: 162–172.
- Lang, J., Winsemann, J., Steinmetz, D., Polom, U., Pollok, L., Böhner, U., Serangeli, J., Brandes, C., Hampel, A. & Winghart, S.**, 2012. The Pleistocene of Schöningen, Germany: a complex tunnel valley fill revealed from 3D subsurface modelling and shear wave seismics. *Quaternary Science Reviews* 39: 86–105.
- Linke, G.**, 1993. Zur Geologie und Petrographie der Forschungsbohrungen qho 1–5, der Bohrung Hamburg-Billbrook und des Vorkommens von marinem Holstein im Gebiet Neuwerk-Scharhörn. *Geologisches Jahrbuch A138*: 35–76.
- Litt, T., Behre, K.-E., Meyer, K.-D., Stephan, H.-J. & Wansa, S.**, 2007. Stratigraphische Begriffe für das Quartär des norddeutschen Vereisungsgebietes. *Eiszeitalter und Gegenwart* 56: 7–65.
- Lutz, R., Kalka, S., Gaedicke, C., Reinhardt, L. & Winsemann, J.**, 2009. Pleistocene tunnel valleys in the German North Sea: spatial distribution and morphology. *Zeitschrift der deutschen Gesellschaft für Geowissenschaften* 160(3): 225–235.
- Mallet, J.-L.**, 2002. *Geomodeling*. Oxford University Press (New York): 624 pp.
- Mangerud, J., Jansen, E. & Landvik, J.Y.**, 1996. Late Cenozoic history of the Scandinavian and Barents Sea ice sheets. *Global and Planetary Change* 12: 11–26.
- Mann, C.J.**, 1993. Uncertainty in geology. In: Davis, J.C. & Herzfeld, U.C. (eds): *Computers in geology – 25 years of progress*. Oxford University Press (Oxford): 241–254.
- Maystrenko, Y., Bayer, U. & Scheck-Wenderoth, M.**, 2005a. The Glueckstadt Graben, a sedimentary record between the North- and Baltic Sea in North Central Europe. *Tectonophysics* 397: 113–126.

- Maystrenko, Y., Bayer, U. & Scheck-Wenderoth, M.**, 2005b. Structure and evolution of the Glueckstadt Graben due to salt movements. *International Journal of Earth Science* 94: 799–814.
- Michelsen, O., Danielsen, M., Heilmann-Clausen, C., Jordt, H., Laursen, G.V. & Thomsen, E.**, 1995. Occurrence of major sequence stratigraphic boundaries in relation to basin development in Cenozoic deposits of the southeastern North Sea. *In: Steel, R.J., Felt, V.L., Johannesen, E.P. & Mathieu, C. (eds): Sequence Stratigraphy of the Northwest European Margin. Special Publications 5, Norwegian Petroleum Society (Stavanger, Norway): 415–427.*
- Michelsen, O., Thomsen, E., Danielsen, M., Heilmann-Clausen, C., Jordt, H. & Laursen, G.V.**, 1998. Cenozoic sequence stratigraphy in the eastern North Sea. *In: Graciansky, P.-C. de, Hardenbol, J., Jacquini, T. & Vail, P.R. (eds): Mesozoic and Cenozoic Sequence Stratigraphy of European Basins. Special Publication 60, Society for Sedimentary Geology (Oklahoma): 91–118.*
- Miller, K.G., Kominz, M.A., Browning, J.V., Wright, J.D., Mountain, G.S., Katz, M.E., Sugarman, P.J., Cramer, B.S., Christie-Blick, N. & Pekar, S.F.**, 2005. The Phanerozoic record of global sea-level change. *Science* 310: 1293–1298.
- Mitchum, R.M., Vail, & Sangree, P.R., 1977, J.B.** Seismic stratigraphy and global changes of sea-level, Part 6: stratigraphic interpretation of seismic reflection patterns in depositional sequences. *In: Payton, C.E. (ed.): Seismic Stratigraphy – Applications to Hydrocarbon Exploration. AAPG Memoir 26 (Houston): 117–133.*
- Møller, L.K., Rasmussen, E.S. & Clausen, O. R.**, 2009. Clinof orm migration patterns of a Late Miocene delta complex in the Danish Central Graben; implications for relative sea-level changes. *Basin Research* 21: 704–720.
- Moreau, J., Huuse, M., Janszen, A., van der Vegt, P., Gibbard, P.L. & Moscarillo, A.**, 2012. The glaciogenic unconformity of the southern North Sea. *In: Huuse, M., Redfern, J., Le Heron, D.P., Dixon, R.J., Moscarillo, A. & Craig, J. (eds): Glaciogenic Reservoirs and Hydrocarbon Systems. Special Publications 368, Geological Society (London): 99–110.*
- Müller, H. & Höfle, H.-C.**, 1994. Die Holstein-Interglazialvorkommen bei Bossel westlich von Stade und Wanhöden nördlich Bremerhaven. *Geologisches Jahrbuch A134: 71–116.*
- Newman, G.A., Hohmann, G.W. & Anderson, W.L.**, 1986. Transient electromagnetic response of a 3-dimensional body in layered earth. *Geophysics* 51(8): 1608–1627.
- Odin, G.S. & Kreuzer, H.**, 1988. Geochronology: some geochronological calibration points for lithostratigraphic units. *Geologisches Jahrbuch A100: 403–410.*
- Ortlam, D.**, 2001. Geowissenschaftliche Erkenntnisse über den Untergrund Bremerhavens. *Bremisches Jahrbuch* 80: 181–197.
- Overeem, I., Weltje, G.J., Bishop-Kay, C. & Kroonenberg, S.B.**, 2001. The late Cenozoic Eridanos delta system in the southern North Sea Basin: a climate signal in sediment supply? *Basin Research* 13: 293–312.
- Paine, J.G. & Minty, B.R.S.**, 2005. Airborne hydrogeophysics. *In: Rubin, Y. & Hubbard, S.S. (eds): Hydrogeophysics. Springer (Dordrecht): 333–357.*
- Palamara, D.R., Rodriguez, V.B., Kellett, J. & Macaulay, S.**, 2010. Salt mapping in the Lower Macquarie area, Australia, using airborne electromagnetic data. *Environmental Earth Sciences* 61: 613–623.
- Panteleit, B. & Hammerich, T.**, 2005. Hydrochemische Charakteristiken und Prozesse im Küstenbereich bei Cuxhaven. *Zeitschrift für Angewandte Geologie* 1: 60–67.
- Paradigm®**, 2011. GOCAD®. Version 2009.3, Patch 2.
- Pharaoh, T.C., Dusar, , Geluk, M., Kockel, M.C., Krawczyk, F., Krzywiec, C.M., Scheck-Wenderoth, P., Thybo, M., Vejbaek, H., & Wees, O.V. van, J.D.**, 2010. Tectonic evolution. *In: Doornenbal, J.C. & Stevenson, A.G., (eds): Petroleum Geological Atlas of the Southern Permian Basin Area. EAGE Publications b.v. (Houten): 25–57.*
- Plink-Björklund, P.**, 2008. Wave-to-tide facies change in a Campanian shoreline complex, Chimney Rock Tongue, Wyoming-Utah, U.S.A. *In: Hampson, G.J., Steel, R.J., Burgess, P.M. & Dalrymple, R.W. (eds): Recent Advances in Models of Siliciclastic Shallow-Marine Stratigraphy. Special Publications 90, Society for Sedimentary Geology (Oklahoma): 265–292.*
- Praeg, D.**, 2003. Seismic imaging of mid-Pleistocene tunnel-valleys in the North Sea Basin – high resolution from low frequencies. *Journal of Applied Geophysics* 53: 273–298.
- Pryet, A., Ramm, J., Chilès, J.-P., Auken, E., Deffontaines, B. & Violette, S.**, 2011. 3D resistivity gridding of large AEM datasets: A step toward enhanced geological interpretation. *Journal of Applied Geophysics* 75: 277–283.
- Rasmussen, E.S.**, 2004. The interplay between true eustatic sea-level changes, tectonics, and climatic changes: what is the dominating factor in sequence formation of the Upper Oligocene–Miocene succession in the eastern North Sea Basin, Denmark? *Global and Planetary Change* 41: 15–30.
- Rasmussen, E.S. & Dybkjær, K.**, 2013. Patterns of Cenozoic sediment flux from western Scandinavia: discussion. *Basin Research* 25: 1–9.
- Rasmussen, E.S., Heilmann-Clausen, C., Waagstein, R. & Eidvin, T.**, 2008. The Tertiary of Norden. *Episodes* 31: 66–72.
- Rasmussen, E.S., Dybkjær, K. & Piasecki, S.**, 2010. Lithostratigraphy of the Upper Oligocene – Miocene succession of Denmark. *Geological Survey of Denmark and Greenland Bulletin* 22: 92 pp.
- Roskosch, J., Winsemann, J., Polom, U., Brandes, C., Tsukamoto, S., Weitkamp, A., Bartholomäus, W.A., Henningsen, D. & Frechen, M.**, 2014. Luminescence dating of ice-marginal deposits in northern Germany: evidence for repeated glaciations during the Middle Pleistocene (MIS 12 to MIS 6). *Boreas*. DOI 10.1111/bor.12083. Wiley-Blackwell (Hoboken).
- Ross, M., Parent, M. & Lefebvre, R.**, 2005. 3D geologic framework models for regional hydrogeology and land-use management: a case study from a Quaternary basin of southwestern Quebec, Canada. *Hydrogeology Journal* 13: 690–707.
- Rumpel, H.-M., Grelle, T., Grüneberg, S., Großmann, E. & Rode, W.**, 2006a. Reflexionsseismische Untersuchungen der Cuxhavener Rinne bei Midlum 2005. *Technischer Bericht, GGA-Institut, Archiv-Nr. 126 015 (Hannover).*
- Rumpel, H.-M., Binot, F., Gabriel, G., Hinsby, K., Siemon, B., Steuer, A. & Wiederhold, H.**, 2006b. Cuxhavener Rinne. *In: Kirsch, R., Rumpel, H.-M., Scheer, W. & Wiederhold, H. (eds): BurVal Working Group: Groundwater resources in buried valleys – a challenge for geosciences. Bonifatius GmbH (Hannover): 227–240.*
- Rumpel, H.-M., Binot, F., Gabriel, G., Siemon, B., Steuer, A. & Wiederhold, H.**, 2009. The benefit of geophysical data for hydrogeological 3D modelling – an example using the Cuxhaven buried valley. *Zeitschrift der deutschen Gesellschaft für Geowissenschaften* 160(3): 259–269.
- Rundberg, Y. & Smalley, P.C.**, 1989. High-resolution dating of Cenozoic sediments from the northern North Sea using ⁸⁷Sr/⁸⁶Sr stratigraphy. *AAPG Bulletin* 73: 298–308.
- Russell, H.A.J., Brennand, T.A., Logan, C. & Sharpe, D.R.**, 1998. Standardization and assessment of geological descriptions from water well records, Greater

- Toronto and Oak Ridge Moraine areas, southern Ontario. *In: Current Research, part E, Geological Survey of Canada, Paper 1998-E: 89–102.*
- Sandersen, P.B.E. & Jørgensen, F.**, 2003. Buried Quaternary valleys in western Denmark – occurrence and inferred implications for groundwater resources and vulnerability. *Journal of Applied Geophysics* 53: 229–248.
- Scheck-Wenderoth, M. & Lamarche, J.**, 2005. Crustal memory and basin evolution in the Central European Basin System-new insights from a 3D structural model. *Tectonophysics* 397: 143–165.
- Sengpiel, K.-P. & Siemon, B.**, 2000. Advanced inversion methods for airborne electromagnetics. *Geophysics* 65: 1983–1992.
- Siemon, B.**, 2001. Improved and new resistivity-depth profiles for helicopter electromagnetic data. *Journal of Applied Geophysics* 46: 65–76.
- Siemon, B.**, 2005. Ergebnisse der Aeroelektromagnetik zur Grundwassererkundung im Raum Cuxhaven-Bremerhaven. *Zeitschrift für Angewandte Geologie* 1: 7–13.
- Siemon, B., Stuntebeck, C., Sengpiel, K.-P., Röttger, B., Rehli, H.-J. & Eberle, D.**, 2002. Characterisation of hazardous waste sites using the BGR helicopter-borne geophysical system. *Journal of Environmental and Engineering Geophysics* 7: 169–181.
- Siemon, B., Eberle, D.G. & Binot, F.**, 2004. Helicopter-borne electromagnetic investigation of coastal aquifers in North-West Germany. *Zeitschrift für geologische Wissenschaften* 32: 385–395.
- Siemon, B., Christiansen, A.V. & Auken, E.**, 2009a. A review of helicopter-borne electromagnetic methods for groundwater exploration. *Near Surface Geophysics* 7: 629–646.
- Siemon, B., Auken, E. & Christiansen, A.V.**, 2009b. Laterally constrained inversion of helicopter-borne frequency-domain electromagnetic data. *Journal of Applied Geophysics* 67: 259–268.
- Siemon, B., Steuer, A., Ullmann, A., Vasterling, M. & Voß, M.**, 2011. Application of frequency-domain helicopter-borne electromagnetics for groundwater exploration in urban areas. *Physics and Chemistry of the Earth* 36: 1373–1385.
- Sørensen, K. & Auken, E.**, 2004. SkyTEM - a new high-resolution helicopter transient electromagnetic system. *Exploration Geophysics* 35: 191–199.
- Sørensen, J.C., Gregersen, U., Breiner, M. & Michelsen, O.**, 1997. High-frequency sequence stratigraphy of Upper Cenozoic deposits in the central and south-eastern North Sea areas. *Marine and Petroleum Geology* 14(2): 99–123.
- Stackebrandt, W.**, 2009. Subglacial channels of Northern Germany – a brief review. *Zeitschrift der deutschen Gesellschaft für Geowissenschaften* 160(3): 203–210.
- Steuer, A.**, 2008. Joint application of ground based transient electromagnetics and airborne electromagnetics. PhD thesis, University of Cologne (Cologne).
- Steuer, A., Siemon, B. & Auken, E.**, 2009. A comparison of helicopter-borne electromagnetics in frequency- and time-domain at the Cuxhaven valley in Northern Germany. *Journal of Applied Geophysics* 67: 194–205.
- Stoker, M.S., Hout, R.J., Nielsen, T., Hjelstuen, B.O., Laberg, J.S., Shannon, P.M., Praeg, D., Mathiesen, A., Weering, T.C.E. van & McDonnell, A.**, 2005a. Sedimentary and oceanographic responses to early Neogene compression on the NW European margin. *Marine Petroleum Geology* 22: 1031–1044.
- Stoker, M.S., Praeg, D., Hjelstuen, B.O., Laberg, J.S., Nielsen, T. & Shannon, P.M.**, 2005b. Neogene stratigraphy and the sedimentary and oceanographic development of the NW European Atlantic margin. *Marine Petroleum Geology* 22: 977–1005.
- Streif, H.**, 2004. Sedimentary record of Pleistocene and Holocene marine inundations along the North Sea coast of Lower Saxony, Germany. *Quaternary International* 112(1): 3–28.
- Tezkan, B., Mbiyah, M.H., Helwig, S.L. & Bergers, R.**, 2009. Time domain electromagnetic (TEM) measurements on a buried subglacial valley in Northern Germany by using a large transmitter size and a high current. *Zeitschrift der deutschen Gesellschaft für Geowissenschaften* 160(3): 271–278.
- Thöle, H., Gaedicke, C., Kuhlmann, G. & Reinhardt, L.**, 2014. Late Cenozoic sedimentary evolution of the German North Sea – A seismic stratigraphic approach. *Newsletters on Stratigraphy* 47(3): 299–329.
- Tølbøll, R.J.**, 2007. The application of frequency-domain helicopter-borne electromagnetic methods to hydrogeological investigations in Denmark. PhD thesis, Department of Earth Sciences, University of Aarhus (Aarhus).
- van der Vegt, P., Janszen, A. & Moscariello, A.**, 2012. Glacial tunnel valleys – current knowledge and future perspectives. *In: Huuse, M., Redfern, J., Le Heron, D.P., Dixon, R.J., Moscariello, A. & Craig, J. (eds): Glaciogenic Reservoirs and Hydrocarbon Systems, Special Publications 368, Geological Society (London): 75–97.*
- Venteris, E.R.**, 2007. Three-dimensional modeling of glacial sediments using public water-well data records: an integration of interpretive and geostatistical approaches. *Geospheres* 3: 456–468.
- Viezzoli, A., Christiansen, A.V., Auken, E. & Sørensen, K.**, 2008. Quasi-3D modeling of airborne TEM data by spatially constrained inversion. *Geophysics* 73(3): F105–F113.
- Walker, R.G. & Plint, A.G.**, 1992. Wave and storm-dominated shallow marine systems. *In: Walker, R.G. & James, N.P. (eds): Facies Models: Response to Sea Level Change. Geological Association of Canada (St John's): 219–238.*
- Wellmann, J.F. & Regenauer-Lieb, K.**, 2012. Effect of geological data quality on uncertainties in geological model and subsurface flow fields. PROCEEDINGS, Thirty-Seventh Workshop on Geothermal Reservoir Engineering Stanford University, Stanford, California, January 30–February 1, 2012 SGP-TR-194.
- West, G.F. & Macnae, J.C.**, 1991. Physics of the electromagnetic induction exploration method. *In: Nabighian, M.N. & Corbett, J.D. (eds): Electromagnetic methods in applied geophysics. Investigations in geophysics, Society of Exploration Geophysicists* 2: 5–45.
- Wiederhold, H., Binot, F. & Kessels, W.**, 2005a. Die Forschungsbohrung Cuxhaven und das „Coastal Aquifer Testfield (CATField)“ – ein Testfeld für angewandte geowissenschaftliche Forschung. *Zeitschrift für Angewandte Geologie* 1: 3–5.
- Wiederhold, H., Gabriel, G. & Grinat, M.**, 2005b. Geophysikalische Erkundung der Bremerhaven-Cuxhavener Rinne im Umfeld der Forschungsbohrung Cuxhaven. *Zeitschrift für Angewandte Geologie* 1: 28–38.
- Wingfield, R.**, 1990. The origin of major incisions within the Pleistocene deposits of the North Sea. *Marine Geology* 91: 31–52.
- Yilmaz, Ö.**, 2001. Seismic data analysis: processing, inversion and interpretation of seismic data. *Society of Exploration Geophysicists (Tulsa): 2027 pp.*
- Zachos, J., Pagani, M., Sloan, L., Thomas, E. & Billups, K.**, 2001. Trends, rhythms, and aberrations in global climate 65 Ma to present. *Science* 292: 686–693.
- Zhdanov, M.S.**, 2010. Electromagnetic geophysics: notes from the past and the road ahead. *Geophysics* 75(5): 75A49–75A66.